gels

MDPI

Review

Steel Slag and Iron Ore Tailings in Cementitious Mine Backfill: Material Functions, Gel Evolution, and Engineering Selection

Zhiheng Nie [1], Fusheng Niu [1,2,*], Jinxia Zhang [1,2], Zeen Yang [1], Yintong Zhang [1], Keqing Li [3], Zehong Cheng [1] and Siqi Zhang [4,*]

[1] College of Mining Engineering, North China University of Science and Technology, Tangshan 063210, China; mktsniezhiheng@foxmail.com (Z.N.); kyky@ncst.edu.cn (J.Z.); yangzeen2001@163.com (Z.Y.); zyt27yu@163.com (Y.Z.); chengzehong@ncst.edu.cn (Z.C.)
[2] Collaborative Innovation Center of Green Development and Ecological Restoration of Mineral Resources, Tangshan 063210, China
[3] School of Resources and Safety Engineering, University of Science and Technology Beijing, Beijing 100083, China; likeqing@ustb.edu.cn
[4] Institute of Mineral Resources, University of Science and Technology Beijing, Beijing 100083, China
* Correspondence: niufusheng@ncst.edu.cn (F.N.); zsq2017@ustb.edu.cn (S.Z.)

Abstract

Steel slag (SS) and iron ore tailings (IOTs) can reduce cement demand in mine backfill, but strength gains may come with greater flow resistance and processing burdens. This review examines how material functions, gel evolution and interfaces connect treatment to engineering performance, and synthesizes criteria for selecting SS–IOT formulations. SS supplies calcium-bearing hydraulic phases and alkalinity, whereas IOT contributes packing, hydrate-bearing surfaces and mineralogy-dependent chemical participation. Silicate gels develop with ettringite and carbonate-bearing hydrates, influencing interfacial bonding and stiffness. Comparison across studies shows that activator response depends on the complete binder formulation and that strength can increase despite bulk pore coarsening. A gentler post-peak decline can accompany lower peak load capacity. Increasing yield stress and decreasing plastic viscosity exert competing effects on pipeline pressure loss. In the reviewed pre-carbonation series, most estimated carbon savings came from composite-binder substitution, with a smaller increment from treating the slag. These findings support treatment selection based on required strength, deformation capacity, transportability and stability, with process burdens and costs assessed for formulations that meet those requirements. Laboratory, pipeline-loop and field evidence inform the successive measurements needed for scale-up.

Keywords: steel slag; iron ore tailings; cemented paste backfill; silicate gels; hydration; activation; rheology; engineering application

Check for updates

Academic Editor: Esmaiel Jabbari

Received: 29 September 2026
Revised: 26 October 2026
Accepted: 5 November 2026
Published: 13 November 2026

Copyright: © 2026 by the authors. Licensee MDPI, Basel, Switzerland. This article is an open access article distributed under the terms and conditions of the Creative Commons Attribution (CC BY) license.

1. Introduction

Cemented mine backfill uses mineral-processing and metallurgical residues to support underground excavations and reduce surface tailings storage [1]. Its placement requires pumpable slurries with controlled bleeding and segregation, followed by sufficient strength for the mining sequence and stable service behavior [2]. Binder demand, preparation costs, and environmental performance consequently influence the selection of mixtures alongside their mechanical properties [3,4].

Steel slag (SS) and iron ore tailings (IOTs) offer complementary material functions. Ca-bearing silicates in SS provide alkalinity and slowly reacting hydraulic constituents [5].

Variable reactivity, poor grindability, and free CaO or MgO nevertheless complicate its use [6–10]. IOT commonly contains quartz and other crystalline silicates with limited accessibility to hydration reactions [11–13]. Its particle-size distribution and morphology support aggregate, packing, and microfilling functions, while mineralogy and processing determine the extent of chemical participation.

Physical and chemical contributions coexist in SS-containing formulations. Some binders harden around tailings that primarily serve as aggregate or filler [14–17]. Grinding and chemical treatment can increase mineral accessibility and the contribution of reactive tailing fractions [11,12,18–20]. These changes are accompanied by competing effects: prolonged grinding can cause agglomeration, excess activator can reduce strength, and extensive carbonation can consume hydraulic slag phases [21–23]. Understanding the resulting performance requires attention to both the treated constituent and the surrounding binder.

A defined literature survey identified 94 original journal and conference papers on cementitious mine backfill containing SS, IOT or both. A Semantic Scholar title/abstract search on 21 October 2026 returned 178 records; deduplication and scope screening retained 84 papers, and checking the existing bibliography added ten. Of the 81 included papers dated through 2025, 60 (74.1%) were published in 2021–2025; another 13 were dated 2026 through the search cutoff. This concentration in recent years supports the need to compare findings across formulations. On 22 October 2026, the 90 records with available Semantic Scholar citation counts had accumulated 1692 citations, with a median of 8.5 per paper; four records had no available count. Supplementary Data S1 provides the search strategy, eligibility decisions, material classifications, annual counts and citation snapshot. These statistics describe the screened literature set.

Existing reviews address SS hydration and activation [6–8], cemented paste backfill (CPB) technology [3,4], and IOT utilization [13,24,25]. The remaining challenge is to connect these material-specific findings to backfill selection when strength, deformation, pore structure and flow respond differently to processing. This review compares those responses across binder formulations, relates them to gel and interface development, and evaluates the additional environmental and economic value of treatment. Backfill studies provide the engineering evidence, while paste, mortar, concrete and model-tailings studies inform the mechanistic interpretation. The synthesis distinguishes peak load capacity from deformation requirements, the competing effects of rheological parameters, and formulation substitution from additional processing benefits. Figure 1 outlines the review.

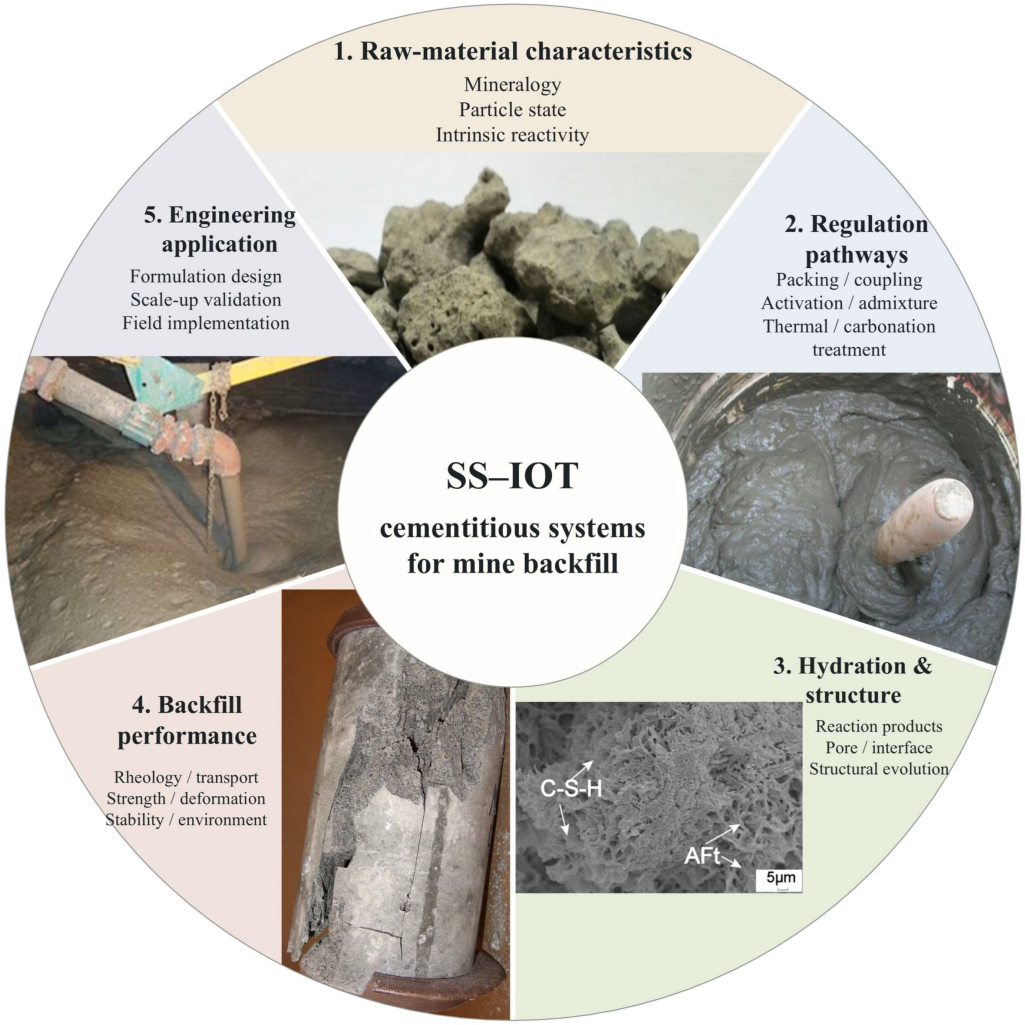


Figure 1. Review scope from raw materials to mine application. Images clockwise: steel slag, [26] (CC BY 4.0); mixing, Tomwsulcer [27] (CC0); IOT interface SEM, [20] (CC BY 4.0); failed concrete cylinder, Xb-70 [28] (public domain); backfill, [29] (CC BY 4.0).

2. Material Characteristics, Coupling, and Activation

2.1. Material States and Functional Complementarity of SS and IOT

Steel slag contains Ca-bearing silicates, ferrite and RO-type phases, with variable amounts of free CaO and MgO [30]. Its hydraulic response depends on the abundance and accessibility of these phases. Dense crystalline particles and slowly reacting constituents generally give SS lower intrinsic reactivity than ordinary Portland cement (OPC) or granulated blast-furnace slag (GBFS) [6–8]. Grinding, sulfate supply, alkalinity and curing can modify its hydration, while reactive Si/Al-bearing constituents help determine which products form [31–33].

IOT mineralogy and particle-size distribution vary among ore sources, although quartz and other silicates are common [34,35]. In quartz-rich tailings, much of the bulk SiO_2 remains within a slowly reacting crystalline framework; processing must improve access to that framework to increase its chemical contribution [11,13,14,18,36]. Hematite itself supplies neither Si nor Al, so the silicate contribution of iron-rich tailings depends on their associated minerals [36]. Figure 2A,B show the SS/IOT XRD patterns and ultrafine-IOT particle-size distribution reported by Zhang et al. [37]. Coarser tailings establish the granular skeleton, whereas finer fractions contribute to packing, void filling and solid–

liquid interfacial area. In a separate SS-based binder study, micro-IOT filled pores promoted hydration-product formation [38].

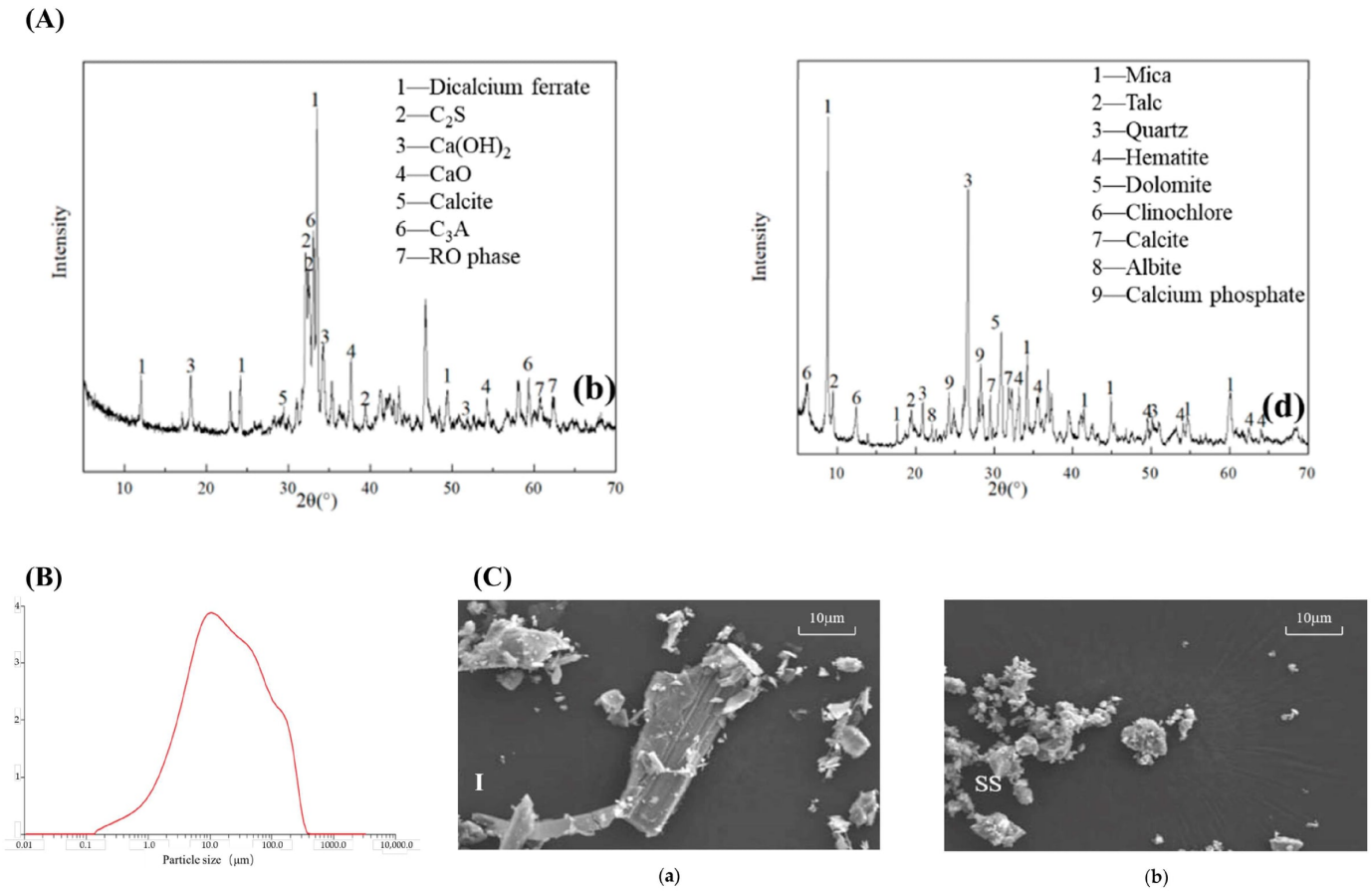


Figure 2. Starting SS and IOT characteristics: (**A**) raw-material XRD patterns of SS (**b**) and IOT (**d**); (**B**) ultrafine-IOT particle-size distribution; (**C**) morphology of IOT (**a**) and SS (**b**). Adapted from Figures 8 and 9 [37] and Figure 4a,b [20] under CC BY 4.0.

Particle size and surface condition affect both the packing of tailings and their contact with pore solution. Refinement changes particle contacts, exposed area and the distribution of water available for hydrate precipitation [39]. Figure 2C shows the starting IOT and SS morphologies [20]. Further grinding can disturb mineral surfaces and expose more of the material to solution [40,41].

SS and IOT are commonly combined with GBFS, gypsum, OPC, fly ash, red mud or phosphorus slag. SS contributes Ca-bearing phases and alkalinity; IOT supplies the granular framework and silicate-bearing surfaces. Reactive aluminosilicates and sulfate-bearing constituents regulate early hydration and gel formation. Binder composition therefore couples particle packing with the availability of Ca, reactive Si/Al, sulfate and water [42,43].

2.2. Coexisting Physical and Chemical Contributions

In many mine-backfill mixtures, an SS-containing binder joins tailings that serve mainly as aggregate [44]. This arrangement accommodates a large tailing fraction even when little of it reacts chemically. Liu et al. obtained a 28 d strength of 29.47 MPa for an optimized SS–blast-furnace-slag (BFS) binder in standard mortar [15]. Backfill made with the same binder reached approximately 1.0–2.8 MPa at 28 d at binder-to-tailings ratios of 1:5–1:10 and 70% solids. The study used total tailings without specifying the ore type. The difference between

mortar and backfill strength illustrates how tailings content and the particle skeleton change the performance delivered by a binder.

Fine IOT changes packing density, water films and particle contacts, as shown in related concrete and mortar systems [45,46]. Its surfaces also provide sites at which hydration products accumulate. In ultrafine-tailings backfill, the increased interfacial area brings a larger fraction of the particles into contact with the binder paste. Packing and hydrate deposition thus operate together, even while substantial crystalline particle cores remain.

Chemical participation becomes more likely when processing exposes or disorders reactive minerals and pore-solution conditions sustain their dissolution [11,12,18–20,22,47,48]. Mechanically activated IOTs formed calcium silicate hydrate in CaO-activated pastes, with ettringite additionally forming when anhydrite was supplied [47]. This supports combining grinding with appropriate calcium and sulfate supply, while the activator response remains composition-dependent [49,50]. Mineral consumption should accompany strength assessment because finer packing can improve strength even when little IOT dissolves.

Within one tailings stream, coarse grains may remain predominantly aggregate, finer grains may improve packing and interfaces, and a smaller reactive fraction may contribute to later hydrates. These functions can occur together rather than replacing one another as treatment proceeds.

The coexisting material functions and their distinct reaction stages are summarized schematically in Figure 3.

Changing SS content also changes the proportion of other binder constituents. Replacing cement with 10% SS increased the 28 d uniaxial compressive strength of cylindrical CPB specimens (50 mm diameter × 100 mm height) from 8.06 to 8.46 MPa; further replacement reduced strength [51]. Binary SS–GBFS pastes instead varied GBFS addition relative to SS mass, with different responses at 3, 7 and 28 d [52]. A third study separately optimized ground granulated blast-furnace slag (GGBFS) and flue-gas-desulfurization (FGD) gypsum at each SS level. Its highest 28 d unconfined compressive strength (UCS) decreased from 2.32 to 0.99 MPa as SS rose from 35 to 55 wt% [53]. Increasing SS supplies Ca-bearing phases but can reduce the fraction of readily reactive clinker or slag [54–56].

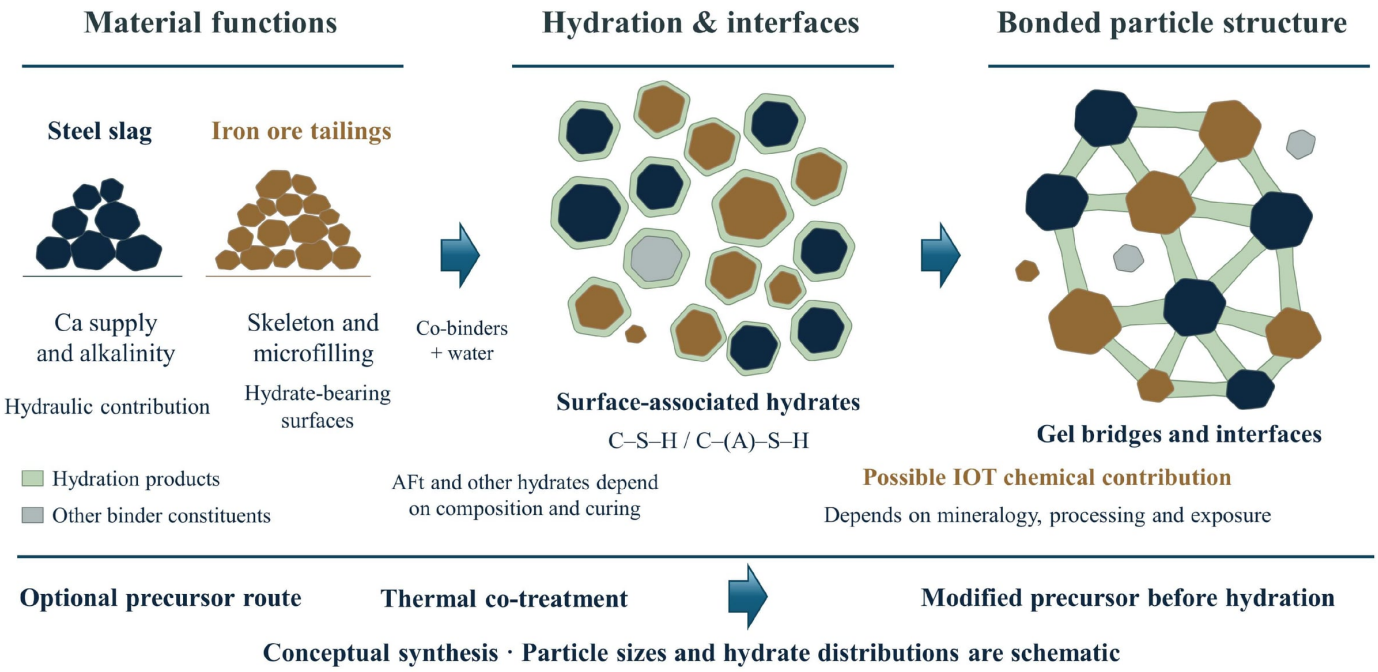


Figure 3. Physical and chemical roles of SS and IOT, showing surface-associated hydrates, interparticle gel bridges and an optional thermal co-treatment route. Author synthesis based on [11,12,18,20,57].

2.3. Mechanical and Chemical Activation

Grinding refines IOT particles and can introduce mineral-surface defects or disorder [58,59]. Increasing ultrafine tailings' specific surface area from approximately 570 to 755 m^2/kg raised 28 d cement–IOT test strength from 24.03 to 34.35 MPa. The strength-based activity index increased from 0.49 to 0.71 [18]. Figure 4 shows the particle-size and SEM morphology shifts; a separate wet-grinding study reported crystallographic disorder [11,22]. Finer particles improve contact and filling, while changes in mineral accessibility can also affect later hydration.

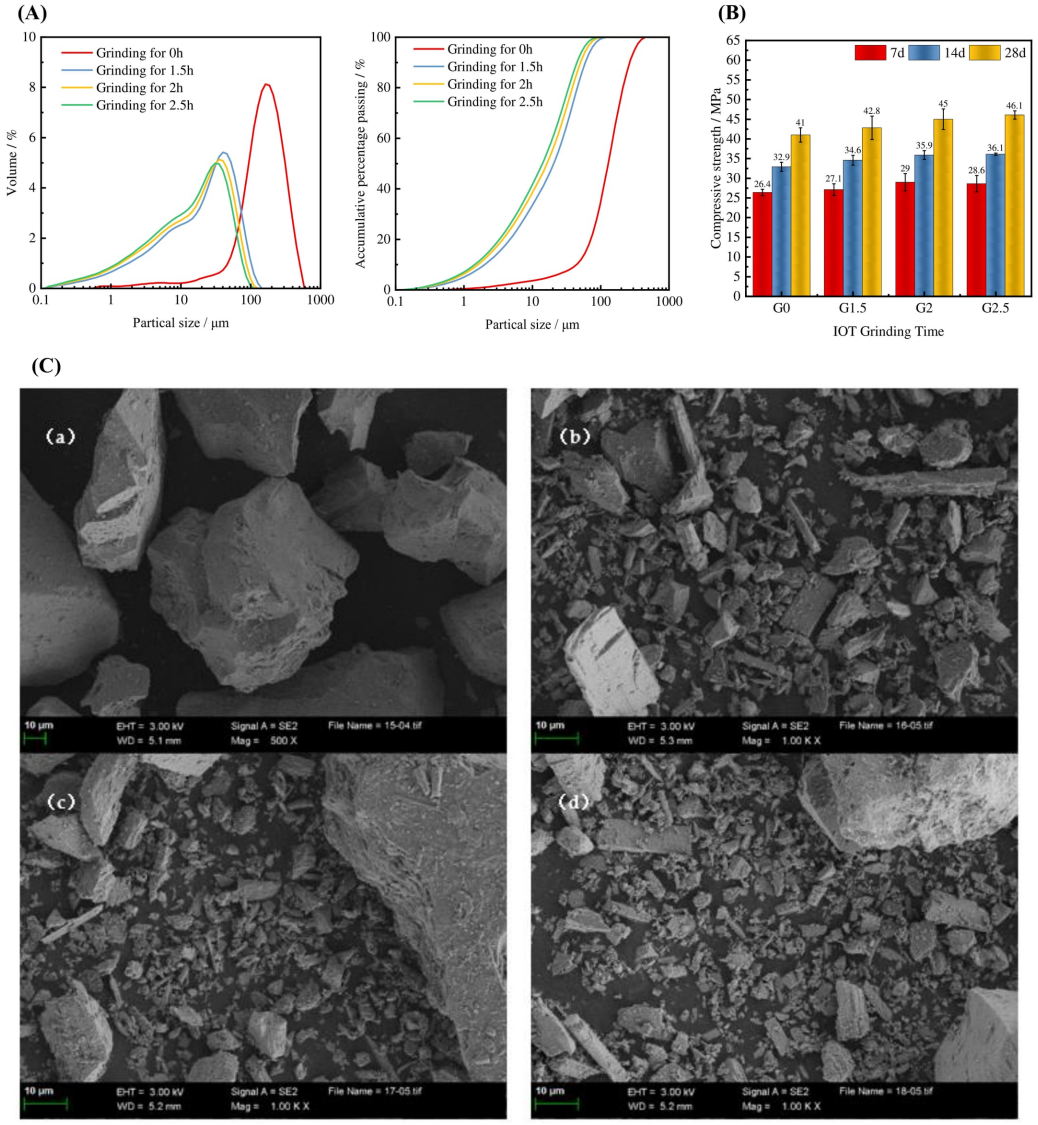


Figure 4. IOT grinding response: (**A**) particle-size distributions; (**B**) concrete compressive strength; (**C**) SEM images of IOT after grinding for (**a**) 0 h, (**b**) 1.5 h, (**c**) 2 h and (**d**) 2.5 h. Adapted from Figures 4c, 5, and 6 [22] under CC BY 4.0.

Zhang et al. reported that extending IOT grinding from 2 to 2.5 h decreased specific surface area from 1587 to 1311 m^2/kg, which they attributed to agglomeration. Over the same interval, additional 28 d strength gain in concrete containing IOT-based composite supplementary cementitious materials (SCMs) was limited (Figure 4B) [22]. A related filler study showed that agglomeration can make part of the nominal particle surface unavailable for calcium silicate hydrate (C–S–H) nucleation [60]. This provides a physical explanation

for why continued size refinement does not necessarily produce a proportional hydration or strength gain.

Wang et al. examined wet-ground micro-IOT in a cement–SS mortar [11]. Grinding reduced crystallinity and changed the measured surface binding energy. Their mixture with 20% SS and 10% micro-IOT reached 50.32 MPa at 28 d, 16.16% above the cement–SS mixture and 93.41% of the cement reference. XRD, thermal and spectroscopic results, together with pore measurements, indicated increased hydration, formation of carbonate-bearing AFm phases (carboaluminates) and a denser paste. Particle refinement thus accompanied changes in both packing and hydrate development. The authors attributed part of the improvement to increased tailings reactivity.

Cui et al. compared separate, mixed and cascade grinding of an SS–GBFS–gypsum–IOT binder at water/binder ratios of 0.50 and 0.35 [61]. Cascade grinding produced higher later-age mortar strengths than the other two routes. The processing sequences changed the relative particle sizes and contacts among constituents, as well as the exposed surfaces.

Chemical activators alter pore-solution chemistry and hydrate precipitation. Alkalis influence dissolution of accessible silicate and aluminosilicate species; sulfate-bearing constituents regulate ettringite (AFt) formation; additional Ca sources modify calcium availability. Organic compounds such as triethanolamine (TEA) can affect complexation and hydration kinetics [12,15,21]. Studies of alkali-activated and salt-containing backfill binders likewise show that the response depends on binder chemistry and the balance among alkalinity, sulfate and reactive constituents [62–64].

Contrasting activator responses occur in cement-based mortars containing 30 wt% composite SCMs. An IOT–SS–fly-ash–GBFS mortar reached 42.9 MPa at 28 d with TEA at 1% of composite SCM mass; higher dosages reduced strength (Figure 5A) [12]. Hu et al. attributed the response to TEA complexation interacting with pozzolanic reaction and nucleation on fine SCM particles. In their interpretation, these processes partly counteract inhibition of silicate hydration. At higher TEA dosages, a proposed Ca–TEA surface layer may hinder C_3S dissolution and C–S–H nucleation, while accelerated aluminate hydration may further delay silicate hydration.

In an IOT–SS–phosphorus-slag mortar, the unactivated mixture had the highest strength, and increasing NaOH or Na_2SiO_3 dosage lowered it (Figure 5B,C) [21]. Zhang et al. proposed that additional alkalinity suppresses cement hydration and that rapid early precipitation on SS and phosphorus-slag particles restricts subsequent reaction; soluble silicate can likewise promote a gel coating that limits further dissolution. The more open microstructure and reduced hydrate development at 28 d are consistent with these interpretations. Activator selection should therefore target sustained hydrate formation by balancing dissolution, precipitation and silicate hydration in the complete blend. Optimum dosage depends on the reactive constituents and the existing pore-solution chemistry.

Mixing water can already contain ions that affect this balance. A CPB study using typical mine-water chlorides found that NaCl and $CaCl_2$ promoted early hydration, whereas $MgCl_2$ lowered solution alkalinity and inhibited it [63]. The effects varied with concentration; $CaCl_2$ also shortened the induction and acceleration periods.

2.4. Thermal Transformation, Carbonation, and Mineralization

High-temperature treatment modifies precursor minerals before hydration [65]. Lian et al. treated molten basic oxygen furnace (BOF) slag with an IOT–limestone modifier, using the available slag heat. Modified slag residues showed a changed mineral assemblage and subsequent activity in pastes containing 70% cement and 30% pristine or modified slag residues [66]. The treatment therefore places IOT within slag reconstruction, with its effect carried forward into the later hydration of the modified precursor.

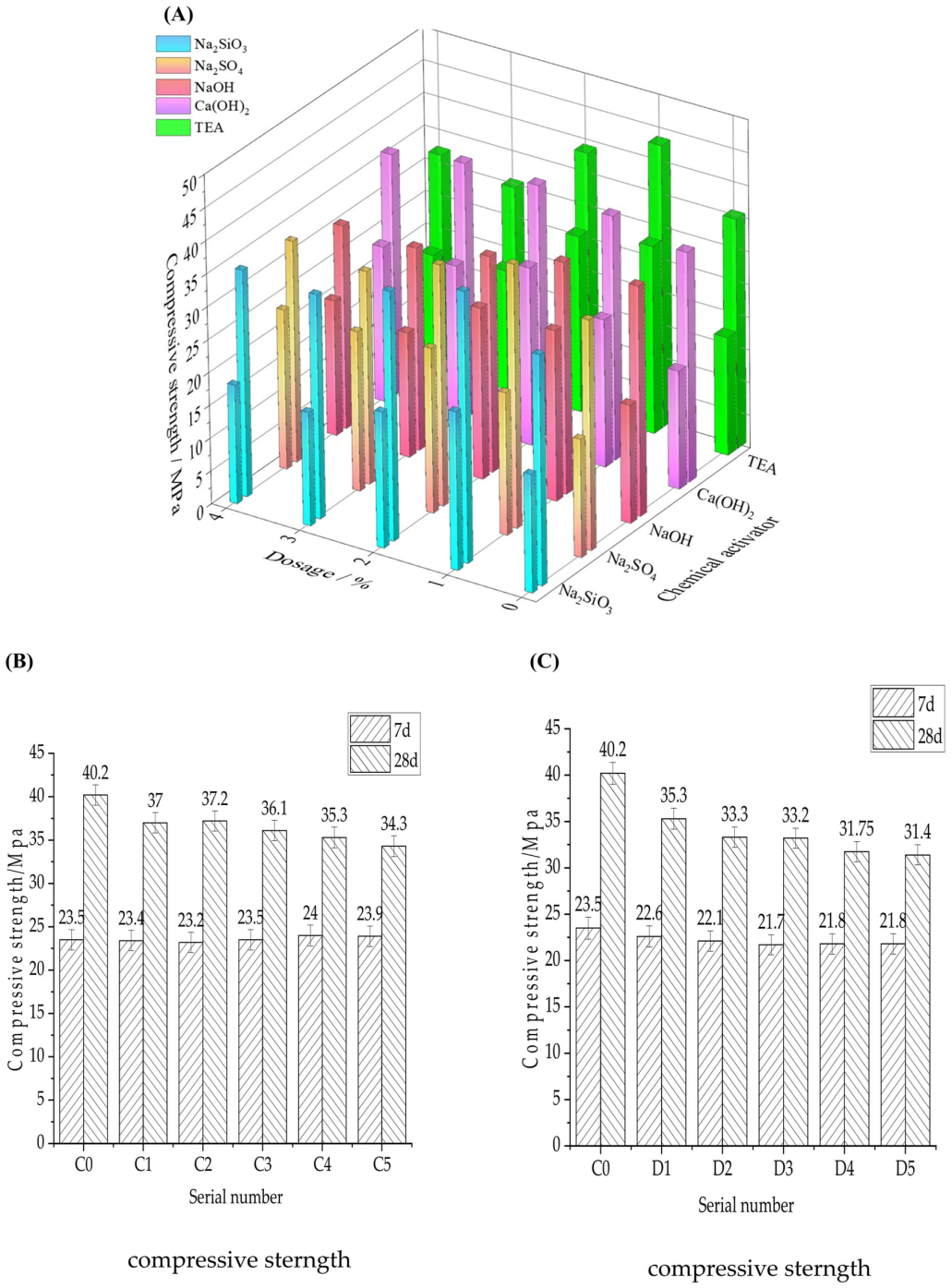


Figure 5. Contrasting chemical-activator responses: (**A**) five activators in an IOT–SS–FA–GBFS composite SCM; (**B**,**C**) NaOH and sodium silicate in an IOT–SS–phosphorus-slag system. Adapted from Figures 6a and 7a [12] and Figure 2 [21] under CC BY 4.0.

Elevated-temperature curing acts on the prepared cementitious mixture [67,68]. Hao et al. cured SS-containing backfill at 20, 40, 60 or 80 °C. Specimens were demolded after 12 h and remained sealed at the respective temperatures until 28 d. Peak strength increased from 3.94 MPa at 20 °C to 5.11 MPa at 60 °C, then fell to 2.87 MPa at 80 °C [69].

SS pre-carbonation changes the precursor through CO_2 uptake and carbonate formation, with corresponding changes in its infrared spectra [23]. The resulting carbonates influence subsequent hydration, while extensive treatment consumes some hydraulic silicate phases [70,71]. In the OPC–metakaolin–SS system, strength rose and then fell as the

extent of slag carbonation increased. Section 3.3 examines the phase assemblage, cement hydration and local mechanical properties associated with that response.

The different treatments leave particles with different surface areas, solution environments and precursor phases. The following section examines how those starting conditions affect reaction kinetics and the gels and crystalline hydrates that subsequently form.

3. Gel and Phase Evolution

3.1. Hydration Kinetics and Reaction Sequence

On contact with water, accessible Ca-, Al-, silicate- and sulfate-bearing constituents establish the solution conditions for dissolution and hydrate precipitation [72]. Li et al. measured different 72 h heat-flow profiles among slag-rich, SS-containing cemented ultrafine-tailings backfill (CUFTB) formulations [73]. Their kinetic model assigned the early reaction to nucleation and crystal growth, followed by increasing influence of phase-boundary interaction or diffusion. In this interpretation, rate control shifts toward reaction at residual precursor interfaces or transports through the developing hydrate layers. The fit describes the 72 h calorimetry window.

In a separate paste comparison, the S3 binder released less heat over 72 h than OPC. Yet backfill prepared with the waste-derived binders achieved higher 28 d strength than the OPC backfill [73]. Li et al. associated the kinetic differences with carbide-slag activation and the supply of reactive BFS. In this system, the lower early heat release was compatible with substantial later hardening.

The SS-containing binder pastes entered the acceleration stage earlier than OPC but released less cumulative heat during the measurement period [16].

Hydration continues beyond the principal heat-release period as precursors react and the hydrate assemblage evolves [74,75]. Early heat flow reflects the reaction rate; later texture reflects cumulative reaction and the locations of precipitation. Continued local precipitation can strengthen particle contacts even at a low overall reaction rate. Linking calorimetry to age-matched phase and interface measurements therefore gives a stronger basis for performance prediction than heat release alone.

3.2. Evolution of Silicate Gels and Sulfate-Bearing Phases

SS-containing binders develop poorly crystalline C–S–H and Al-bearing calcium aluminosilicate hydrate (C–(A)–S–H) together with crystalline hydrates, including AFt [76]. Their composition and intergrowth vary with precursor chemistry, sulfate supply and curing age [12,20,37,61,73]. Studies of model cementitious gels place Al in silicate-chain environments and show that Ca and alkalis participate in charge compensation [77–79]. Changes in Al and alkali availability therefore alter local gel structure as well as composition.

Activator chemistry changed the 28 d thermal response of a cement-based mixture containing 30 wt% composite SCMs [12]. Of the tested Na_2SiO_3, Na_2SO_4, NaOH, $Ca(OH)_2$ and TEA additions, TEA gave the largest low-temperature mass-loss response and the highest strength. The accompanying 7/28 d XRD and FTIR spectra and selected 28 d SEM images (Figure 6) show how the activator series changed the hydrate assemblage and texture. Thermal measurements are consistent with greater development of gel/AFt-bearing hydrates and a change in portlandite evolution in that mixture.

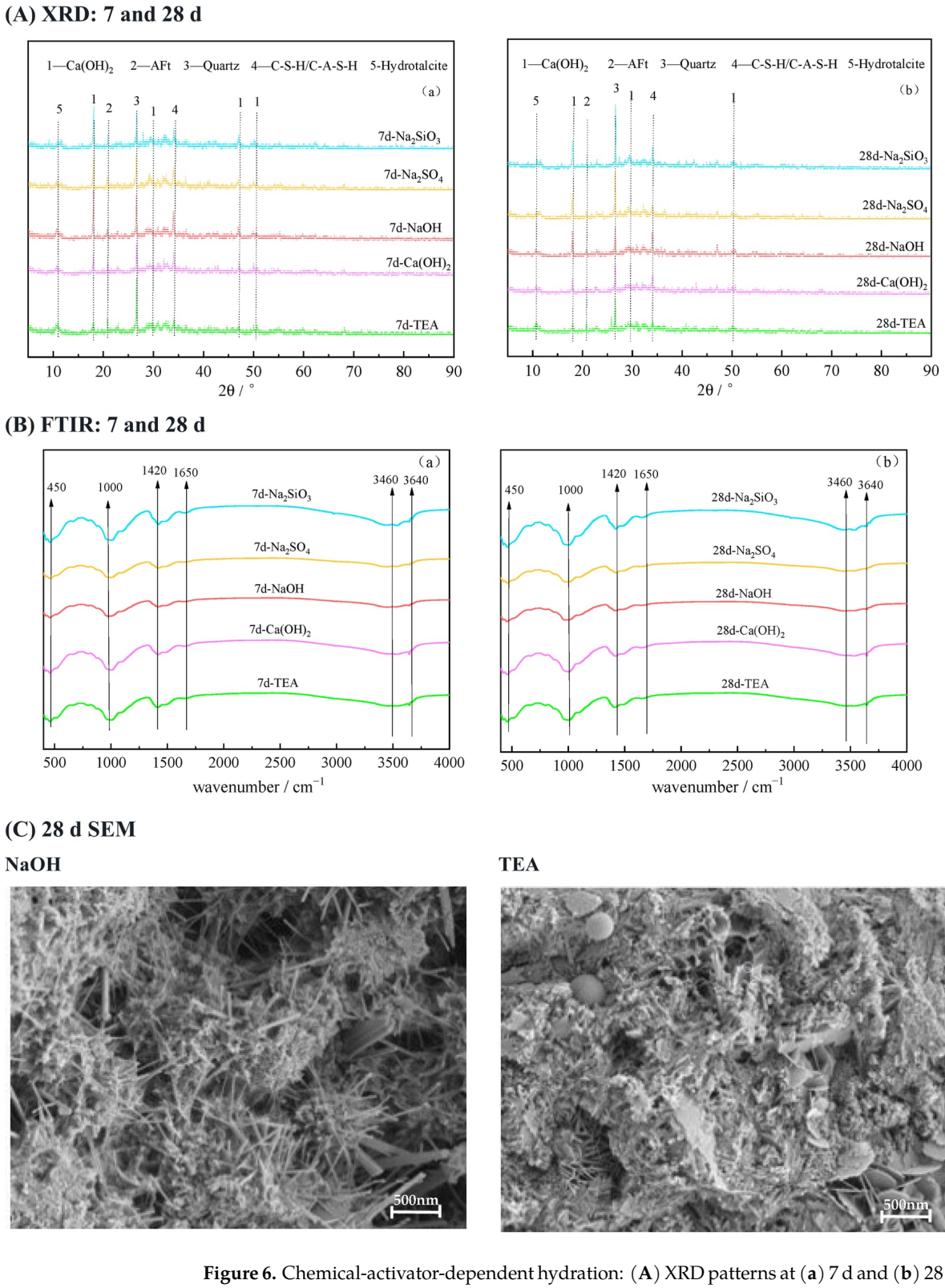


Figure 6. Chemical-activator-dependent hydration: (**A**) XRD patterns at (**a**) 7 d and (**b**) 28 d; (**B**) FTIR spectra at (**a**) 7 d and (**b**) 28 d; (**C**) SEM images at 28 d after NaOH (**left**) and TEA (**right**) activation. Adapted from Figures 3, 4 and 7c,e [12] under CC BY 4.0.

The SS–FGD-gypsum–FGD-ash–ultrafine-tailings binder developed a more connected hydrate assemblage with age [37]. The XRD and FTIR evidence in Figure 7 indicated silicate-gel development and polymerization together with continued AFt formation. Zhang et al. attributed the sustained sulfate supply partly to sulfite oxidation in the FGD ash. Between 28 and 90 d, SEM images showed further gel wrapping and intergrowth with

AFt. Total TG mass loss increased between 3 and 28 d, including hydrate dehydration and carbonate/sulfite decomposition. This case links continuing reactant supply to progressive gel–crystal connections, providing a spatial explanation for later hardening beyond early reaction-rate differences.

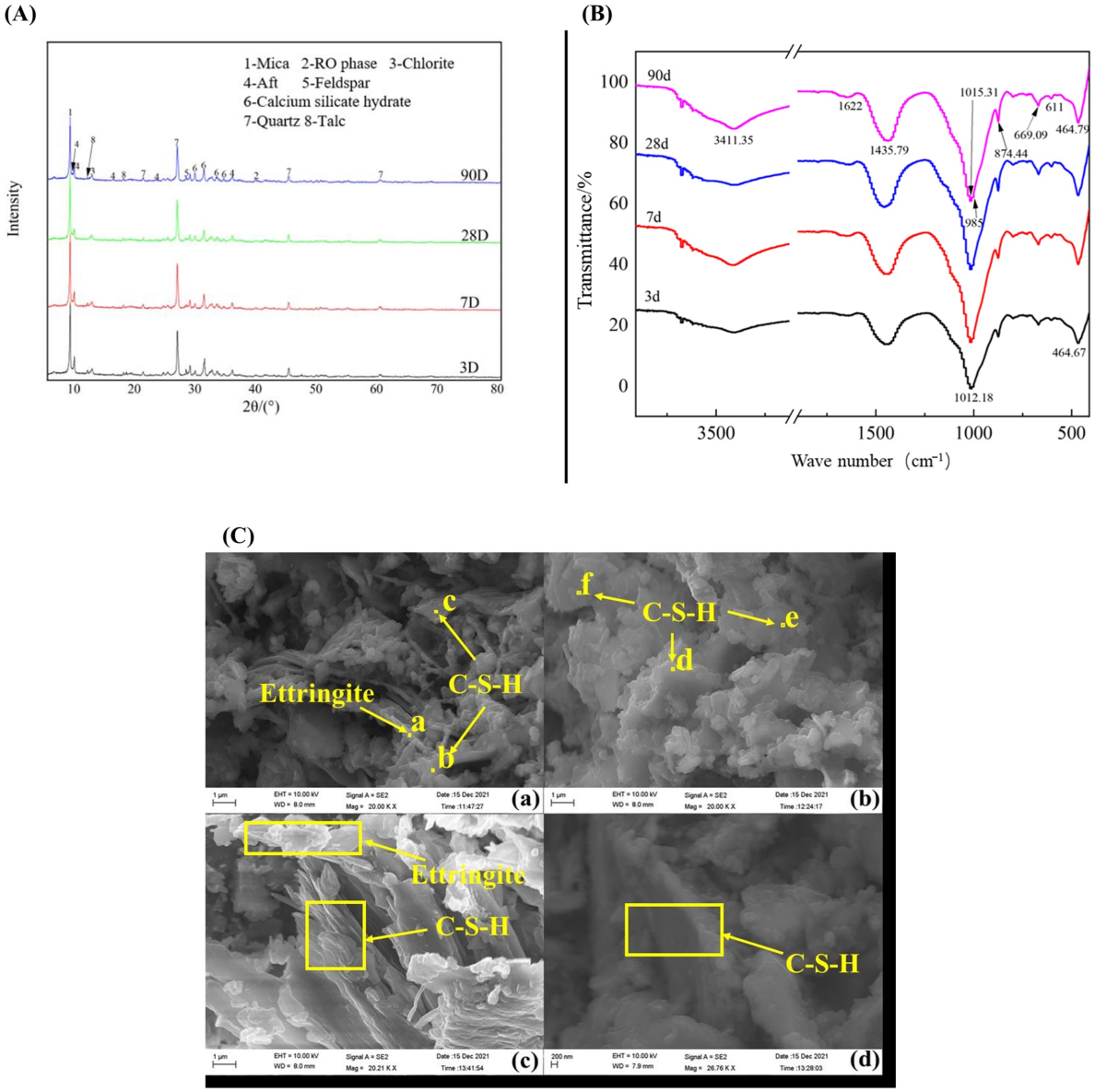


Figure 7. Age-dependent hydration of an SS–FGD-residue–ultrafine-tailings binder: (**A**) XRD; (**B**) FTIR; (**C**) SEM images at 28 d (**a**,**b**) and 90 d (**c**,**d**). Adapted from Figures 3–5 [37] under CC BY 4.0.

Li et al. examined another blend containing SS, fly ash, BFS, carbide slag and gypsum [73]. Pure-binder XRD at 7 and 28 d identified AFt and calcite. In CUFTB-S4, the 3 and 28 d micrographs show products developing around the tailings, and SEM–EDS spots were interpreted as low-Ca, Al-bearing gels containing Na or K. This study captures early hydrate development and local compositional variation; the later-age images from the separately studied formulation in Figure 7 show continued gel–AFt intergrowth [37,73].

Gypsum and sulfate-bearing residues can sustain AFt formation beyond early hydration [37,73,80]. Sulfate availability also changes the distribution of Al among hydrates [81]. In metakaolin–limestone blends, hemicarboaluminate (Hc) and monocarboaluminate (Mc) formed after the principal silicate and aluminate heat-release events and contributed to pore

refinement and strength; with sufficient sulfate, metakaolin-derived Al also contributed to AFt [82]. Comparisons with limestone–slag blends indicated differences in gel composition and later Hc-to-Mc conversion [83]. The aluminosilicate source and sulfate–carbonate supply therefore influence both gel and crystalline-hydrate formation.

Studies of synthetic calcium aluminosilicate hydrates link Al-associated chain cross-links to stiffness [84], while C–S–H nanomechanics also depend on interlayer densification [85]. Solid-state nuclear magnetic resonance provides complementary information on local structures and their evolution [86]. These structure–property relationships help interpret the gel-associated mechanical responses considered below.

3.3. Carbonate-Driven Phase Redistribution and Gel Micromechanics

Carbonation alters subsequent silicate hydration and the distribution of Al-bearing hydrates [83,87,88]. Su et al. used binders containing 40 wt% OPC, 30 wt% metakaolin and 30 wt% untreated or pre-carbonated SS in their carbon-reducing mine backfill (CRMB) series. CRMB0 denotes the untreated-slag reference; CRMB1–CRMB4 contain slag pre-carbonated for 10, 20, 30 and 120 min (approximately 30%, 50%, 85% and 100% carbonation), respectively [23]. Carbonate availability promoted Hc and Mc alongside AFt. At moderate pre-carbonation, carbonate-bearing products provided additional hydration interfaces while reactive silicates remained available for subsequent hardening.

At the greatest extent of pre-carbonation, the later hydration response became less favorable. CRMB4 contained more calcite and unhydrated silicate phases than CRMB2 at 28 d, and its reported cement degree of hydration was lower [23]. The treatment had therefore changed both the phases introduced with the slag and the subsequent reaction of the composite binder.

Su et al. related the non-monotonic response to changes already present in the carbonated precursor [23]. Ca-bearing phases dissolved or decalcified during treatment, forming carbonates and silica-rich material. Moderate carbonation retained hydraulic silicates alongside the finer carbonate-bearing and gel-like products. After mixing with OPC and metakaolin, the new surfaces supported nucleation and precipitation while the remaining silicates could continue to hydrate. More extensive treatment accumulated carbonate and consumed more of the original silicate constituents. The useful balance therefore involved both the products created by carbonation and the reactive precursor left afterward.

The thermal results help explain the later phase assemblage. At the measured ages, carbonated-slag binders contained less portlandite than the untreated-slag binder [23]. Su et al. attributed this reduction to reaction of portlandite with the silica-rich carbonation products. OPC hydration continued to supply portlandite, however, so the measured content reflected simultaneous production and consumption. Carbonate species also diverted part of the aluminate reaction toward Hc and Mc while AFt remained present. A phase fraction could therefore change differently from the cement hydration degree or strength. The QXRD and thermal measurements describe these coupled reactions in a binder containing 30 wt% metakaolin, whose Al supply is central to interpreting the carboaluminate response.

Nanoindentation clustering of 28 d binder pastes identified populations assigned to low-density (LD) and high-density (HD) C–S–H. Their highest elastic moduli occurred in CRMB2, increasing by 22.1% and 41.3%, respectively, relative to CRMB0. Moderately carbonated formulations also showed improved hardness, whereas both parameters fell below the untreated reference in CRMB4 [23]. CPB prepared at a binder-to-tailings mass ratio of 1:6 and 68% solids reached its highest 28 d strength in CRMB2: 4.11 MPa. The corresponding values were 3.30 MPa for CRMB0 and 3.90 MPa for OPC [23]. The strength response thus coincided with changes in carbonate-bearing phases, subsequent hydration and local gel-associated mechanical properties.

3.4. IOT Contributions Within Multicomponent Reaction Networks

IOT supplies particle surfaces and, where minerals react, dissolved constituents to the binder. OPC, SS, slag, fly ash and red mud can supply some of the same chemical species [89]. The studies in this section describe interfacial hydrate deposition, mineral changes during later hydration and precursor transformation before hydration.

IOT surfaces provide substrates on which hydration products can accumulate [90]. Hu et al. observed C–S–H-type products adhering to relatively intact IOT particles and suggested a nucleation-substrate role with limited direct chemical participation (Figure 8) [20]. The paste FTIR spectra in Figure 8 characterize bond-structure changes in the hydrated multicomponent binder. Together, the images and spectra describe hydrate development around particles whose crystalline cores remain largely preserved.

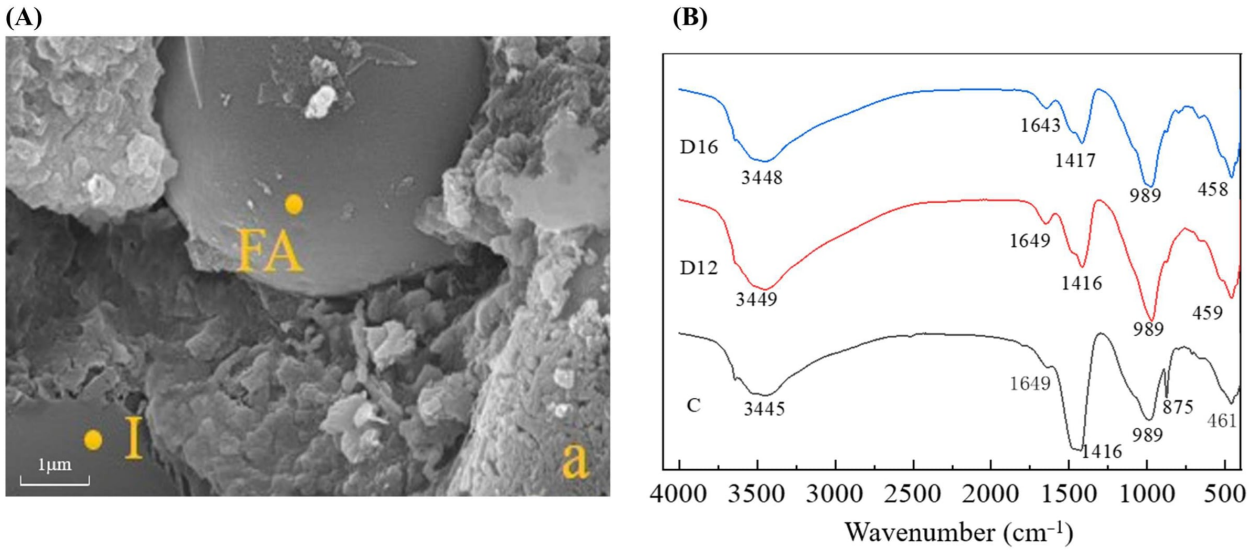


Figure 8. IOT interface and hydrated-binder chemistry: (**A**) D16 interface SEM at 28 d; (**B**) FTIR spectra of C, D12 and D16. Adapted from Figures 10 and 13 [20] under CC BY 4.0.

Hu et al. also compared dissolved Ca, Si and Al in SS-, slag- and fly-ash-containing systems and proposed an IOT-derived Si contribution from mineralogical changes [20]. Their surface observations and solution results answer different questions: hydrate deposition locates interfacial growth, while mixed-binder solution chemistry records contributions from several precursors.

In an ultrafine-tailings binder, Zhang et al. associated age-dependent mineral changes and later silicate-gel development with increasing tailings participation (Figure 7) [37]. Taken together, these studies support coexisting surface deposition and possible mineral reaction, but quantify neither as an IOT-derived fraction. Attribution requires a measured loss of identified IOT minerals to be reconciled with the dissolved and precipitated inventories. Section 5.3 sets out the corresponding measurements.

Where IOT contains calcite, a further chemical pathway is available through carbonate–aluminate reactions. Established calcite chemistry indicates formation of carbonate-bearing AFm and a changed AFm/AFt balance, governed by Al and sulfate availability [88]. Thus, the relevant participation conditions differ among quartz-rich, carbonate-bearing and iron-rich tailings. Aggregate and microfilling functions can persist alongside these phase-specific reactions.

4. Microstructure and Engineering Performance

4.1. Pore Architecture, Interfacial Structure, and Cracking

Hydration links particles into a load-bearing structure, while pore evolution affects the strength of sulfate-containing backfill [91]. Pores and interfaces need not evolve in parallel. Pore-size distribution, interfacial bonding and crack development provide complementary explanations for the mechanical response of SS-containing mixtures.

Long-term SS–GBFS–gypsum backfill tests show that UCS rose from 3.55 MPa at 28 d to approximately 5.5 MPa at 365 d, while mercury intrusion porosimetry (MIP)-derived porosity increased from 29.81% to 46.86% and pores became coarser [92]. An increase in mercury-accessible pore volume therefore did not imply a loss of load-bearing capacity. Xiao et al. interpreted this response as the combined effect of hydrate self-consolidation strengthening the paste and interfaces, sulfate-related pore coarsening, and differences in pore geometry, location and connectivity.

The importance of pore location is illustrated by 28 d concrete containing IOT-based composite SCMs [22]. Across the IOT grinding series, MIP indicated greater matrix pore volume and coarser pores, whereas backscattered-electron images and image analysis showed narrower cracks and lower porosity in the interfacial transition zone (ITZ; Figure 9). Local interfacial densification thus coexisted with matrix pore coarsening. Zhang et al. related this distinction to the role of the ITZ in transferring stress between the matrix and aggregate.

Other CPB studies associate higher strength with pore refinement or reduced porosity [91,93]. Together, these studies distinguish two forms of decoupling: strength and pore volume can diverge during aging, and matrix and interface porosity can respond differently to the same processing change. Strength assessment consequently requires pore structure, bonded contacts and cracking to be compared with mechanical response at matched ages and curing conditions. Bulk porosity alone cannot identify the controlling contribution.

4.2. Strength, Deformation, and Failure Response

Peak strength and deformation capacity provide different criteria for backfill selection. Stress–strain curves resolve the approach to peak load and the resistance retained during continued deformation, while failure morphology identifies how the bonded skeleton breaks down [94–97].

Hao et al. [51] tested 28 d SS–cement–IOT cylinders (50 mm diameter × 100 mm height) at 1 mm/min. Their curves pass through initial compaction, approximately linear loading, nonlinear pre-peak deformation and post-peak softening. The cement reference showed a steep post-peak drop; 10–20% SS produced double-peaked responses, while 30–60% SS gave a more gradual descent. Peak strain increased with SS content, although UCS fell from 8.46 MPa at 10% SS to 2.42 MPa at 60%. Thus, a gentler post-peak decline can accompany a substantial reduction in absolute load capacity. Mixture selection requires both the target peak resistance and the stress retained at the anticipated deformation. The transition from predominantly splitting to combined splitting and local shear further distinguishes the 30–60% SS mixtures.

In a separate copper-tailings and Portland-cement CPB system, Zhang and Li documented different failure morphologies at 7, 14 and 28 d under 300 kPa triaxial compression (Figure 10) [98]. At 28 d, the reported failure developed from an inclined shear plane toward an X-shaped pattern.

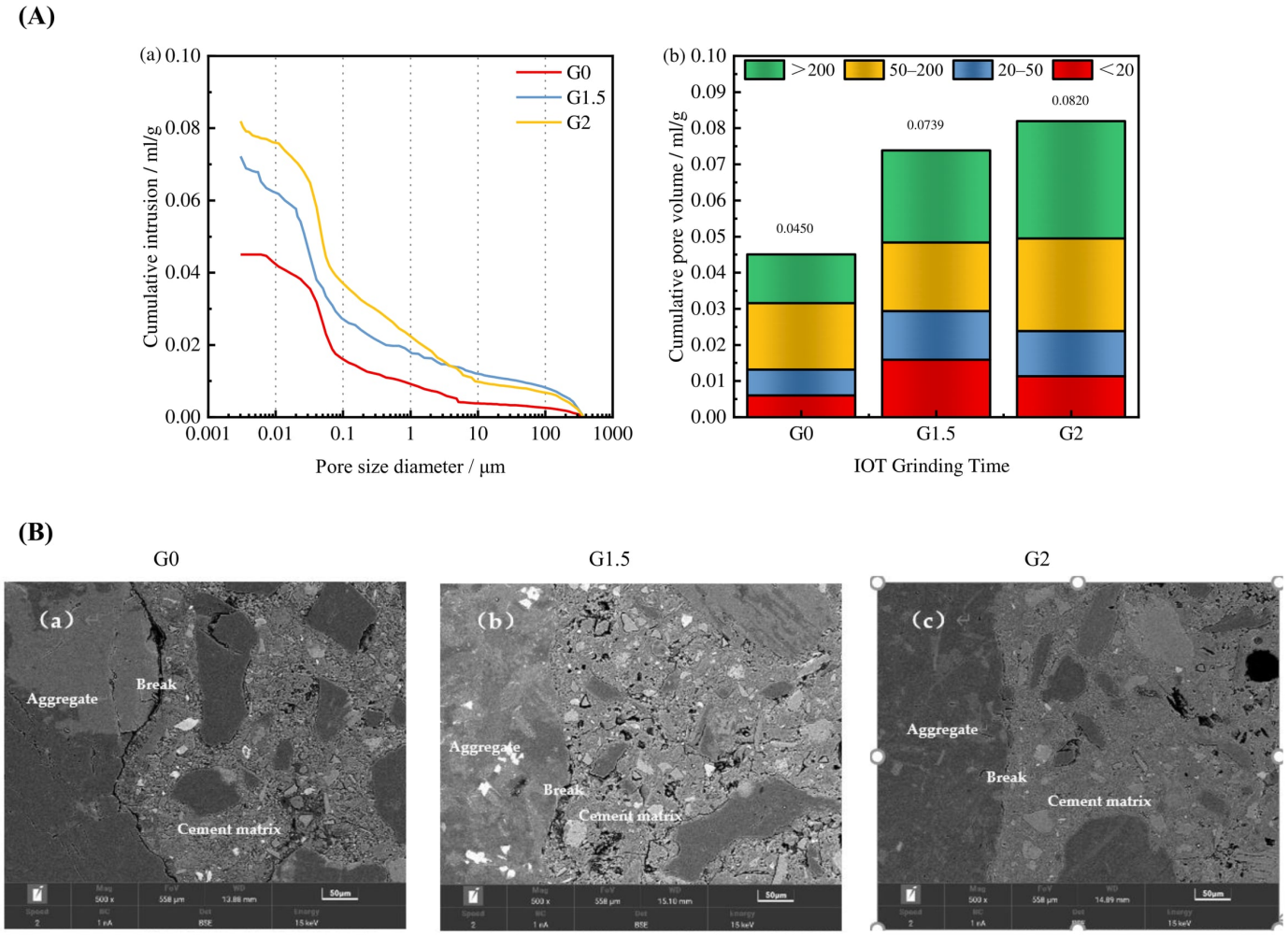


Figure 9. Matrix pores and ITZ in IOT composite-SCM concrete at 28 d: (**A**) MIP results showing (**a**) cumulative intrusion volume and (**b**) pore volume distributions by pore-size range; (**B**) BSE interface images of (**a**) G0, (**b**) G1.5 and (**c**) G2, corresponding to IOT grinding times of 0, 1.5 and 2 h, respectively. Adapted from Figures 9 and 11a–c [22] under CC BY 4.0.

Compression, direct tension and direct shear define a broader strength envelope [94,96,97]. For conventional CPB, Pan and Grabinsky found that a Mohr–Coulomb envelope consistently described these strengths. In their direct-shear study, increasing normal stress changed post-peak response from dilative softening to contractive hardening [95]. The strength envelope describes the failure threshold; predicting subsequent deformation also requires the evolution of resistance and volume change. For SS–IOT backfill, calibration should therefore include stiffness, peak strain and post-peak stress retention under the relevant stress path. This connects mixture selection to the deformation imposed by the surrounding rock.

Volume stability adds a separate service constraint. Free CaO/MgO and delayed reactions can affect slag-containing materials [99], while a high-SS field study reported local cracking [52].

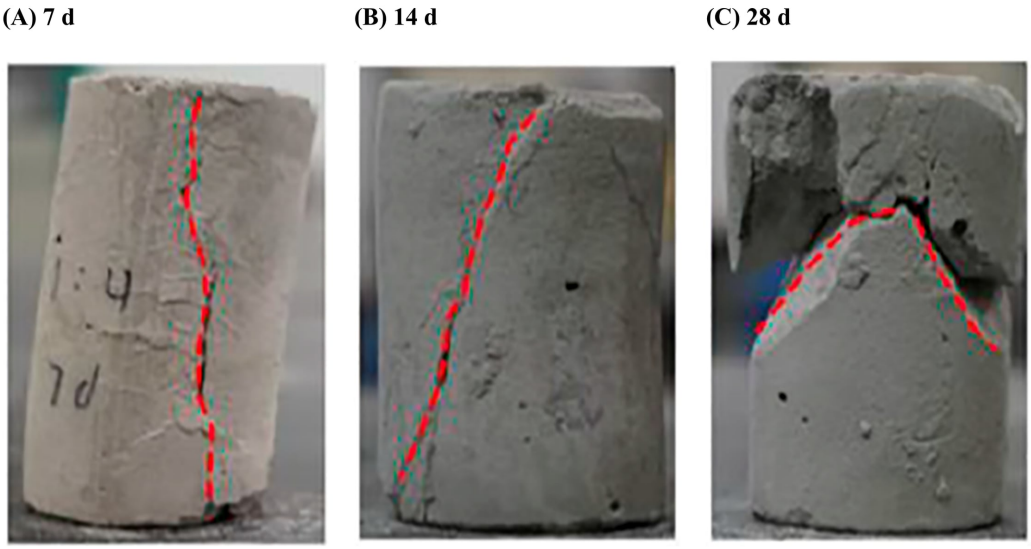


Figure 10. Failure morphologies of conventional cemented paste backfill with 25% cement under 300 kPa triaxial compression: (**A**) 7 d; (**B**) 14 d; (**C**) 28 d. The colored lines trace the visible cracks on the specimen surfaces. Adapted from Figure 7 [98] under CC BY 4.0.

4.3. Rheology, Transportability, and Fresh-State Stability

Fresh-state properties control whether a selected mixture can be mixed, transported and placed. The solids concentration, binder-to-tailings ratio, particle shape and fines affect yield stress, plastic viscosity, slump and bleeding [100–102]. Changes intended to improve hardened strength can therefore alter flow resistance during placement.

At a binder-to-tailings ratio of 1:4, Yang et al. increased solids concentration from 68 to 72% [103]. The 28 d strength rose from 2.66 to 3.53 MPa, while slump fell from 26.2 to 23.6 cm and bleeding from 9.4 to 6.3%. A separate validation mixture at 72% solids reached 1.74 MPa at 7 d and 3.61 MPa at 28 d, with a slump of 24.2 cm and bleeding of 5.91%.

Cai et al. obtained a 28 d strength of 5.90 MPa at 72% solids in an SS–desulfurization-ash–GBFS–IOT formulation containing 20% SS and 20% desulfurization ash in the binder [17]. The associated testing sequence is shown in Figure 11. The expansion-test response surfaces (Figure 12) indicated that increasing SS raised yield stress and lowered plastic viscosity; increasing desulfurization ash produced the reverse trends under the fitted test conditions. Binder substitutions thus affected the resistance to flow initiation and the subsequent flow behavior differently.

To translate these competing changes into transport resistance, the straight-pipe Bingham approximation used by Cai et al. [17] can be written as

$$G = \frac{\Delta P}{L} = \frac{16\tau_0}{3D} + \frac{32v\eta_0}{D^2} \quad (1)$$

Here, G is pressure gradient, D is pipe diameter, v is mean flow velocity, and τ_0 and η_0 are yield stress and plastic viscosity. At fixed D and v, formulation-to-formulation changes, denoted by δ, satisfy

$$\delta G = \frac{16}{3D}\delta\tau_0 + \frac{32v}{D^2}\delta\eta_0 \quad (2)$$

Within this approximation, when $\delta\tau_0 > 0$ and $\delta\eta_0 < 0$, the pressure gradient decreases only if $-\delta\eta_0 > \frac{D\delta\tau_0}{6v}$. A lower plastic viscosity therefore does not guarantee a lower pressure gradient. This comparison requires parameters obtained using the same method under comparable conditions. Pipe geometry and operating conditions also enter transport assessment [104].

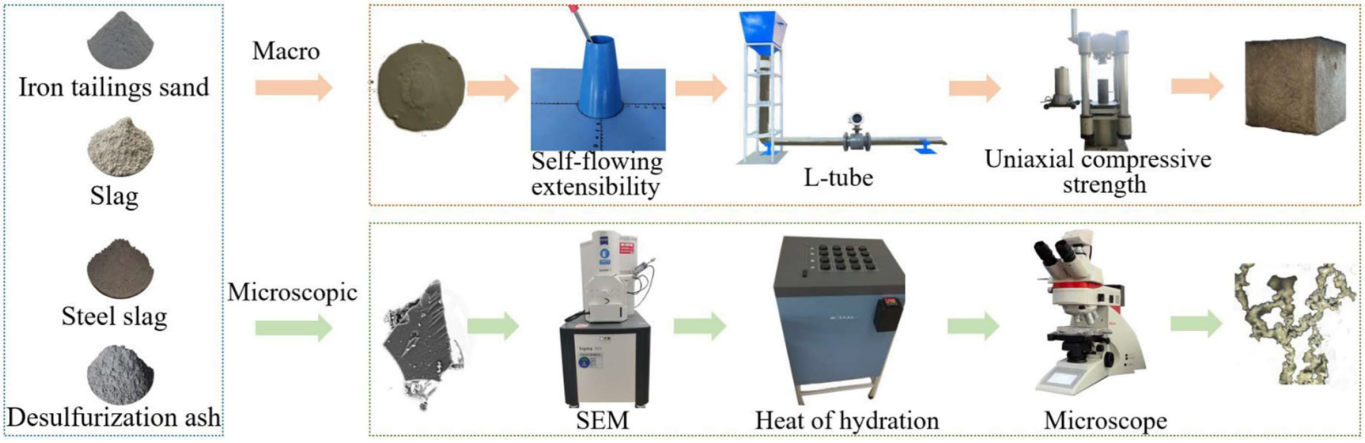


Figure 11. Experimental testing sequence for the SS–IOT–GBFS–desulfurization-ash slurry. Orange arrows indicate the macroscopic testing route, and green arrows indicate the microstructural characterization route. Reproduced from Figure 4 [17] under CC BY 4.0.

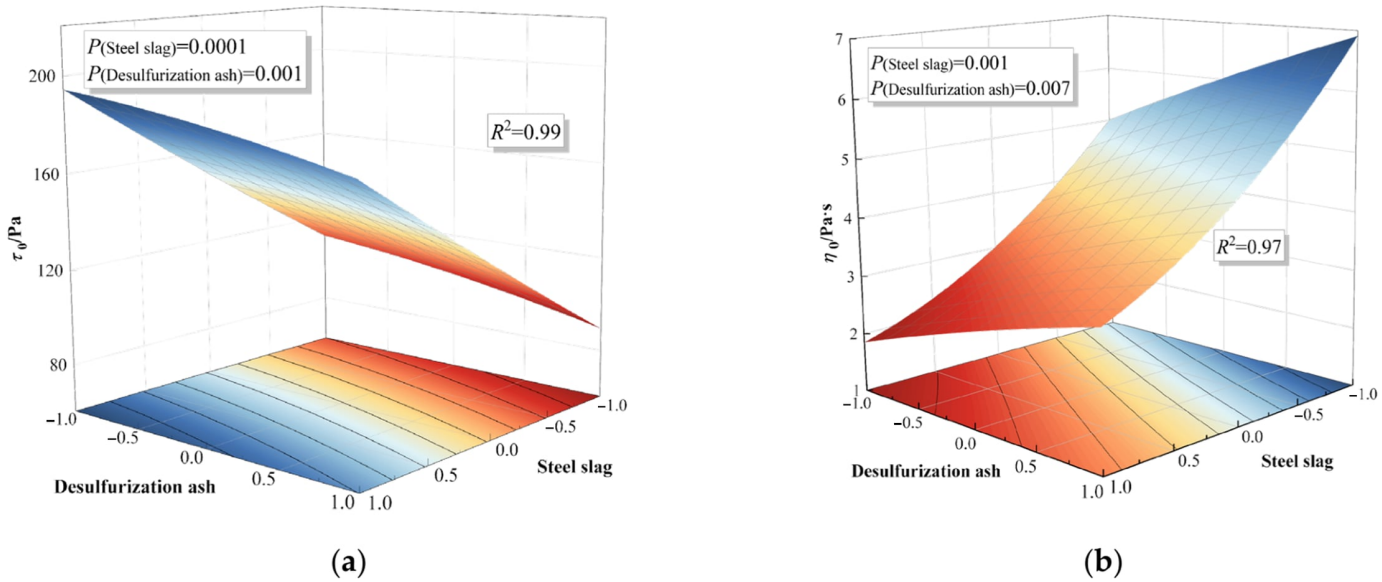


Figure 12. Fitted expansion-test responses of (**a**) yield stress and (**b**) plastic viscosity to coded SS and desulfurization-ash factors. Reproduced from Figure 7 [17] under CC BY 4.0.

Cai et al. [17] reported loop-derived yield stress and plastic viscosity values of 134.2 Pa and 2.96 Pa·s for the selected solid-waste slurry, compared with 98.68 Pa and 0.66 Pa·s for the OPC reference. At the same pipe diameter and flow velocity, these reported parameters predict a higher straight-pipe pressure gradient within the adopted Bingham approximation. The parameter-based ranking differs from that suggested by the labeled pressure histories in Figure 13C, so the experimental comparison remains uncertain.

Increasing solids or binder content can raise strength and reduce bleeding at the expense of flowability. With ultrafine tailings, the concentration that can be maintained in operation also depends on thickening and slurry handling [105]. These production constraints are examined in the field cases below.

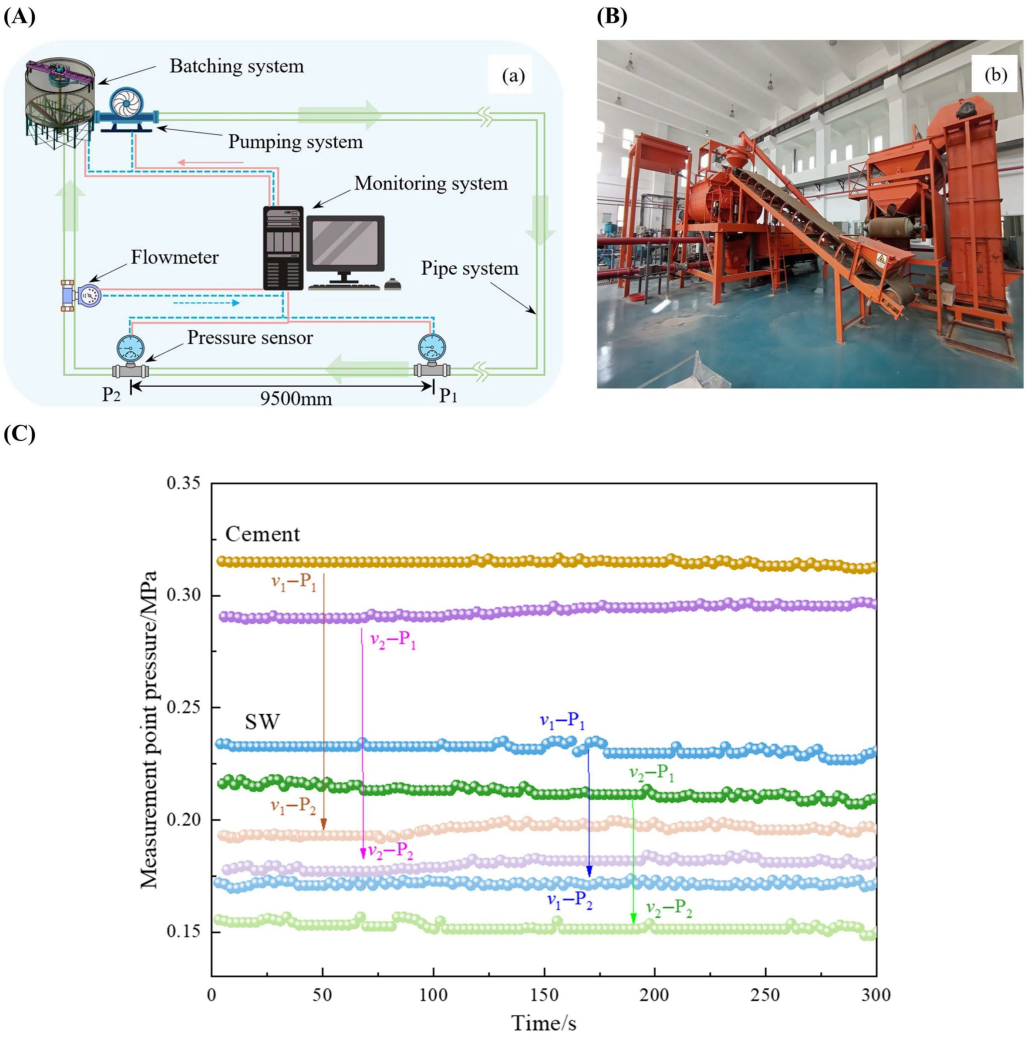


Figure 13. Semi-industrial slurry transport: (**A**)(**a**) 30 m loop system; (**B**)(**b**) slurry preparation and pumping equipment; (**C**) pressure histories at 0.5 and 0.6 m s^{-1}. In panel (**A**), green arrows indicate the slurry circulation direction. In panel (**C**), the colored curves represent pressure measurements at P_1 and P_2 under the indicated materials and flow velocities; the arrows point to the corresponding traces. Adapted from Figures 17a,b and 18 [17] under CC BY 4.0.

5. Engineering Design, Field Application, and Future Needs

5.1. From Formulation Screening to Field-Ready Backfill

Backfill development begins with binder selection and testing of tailing-rich mixtures. The standard-mortar and backfill results in Section 2.2 show how strength changes when a binder is used with a large tailing fraction [15]. Formulation trials then establish workable combinations of binder dosage and solids concentration, including the strength, slump and bleeding results described in Section 4.3 [103]. Representative formulations and their reported performance are summarized in Table 1.

Loop testing informs pipe and pumping selection, while field operation additionally tests thickening, storage, mixing and placement [17].

Hu et al. reported mine filling with ultrafine tailings having a median size of approximately 21.2 μm and more than 80% of particles below 75 μm [105]. Their preparation system combined thickening, storage and two-stage mixing to manage the fine slurry. At a binder-to-tailings ratio of 1:4 and approximately 58–60% solids, continuous filling lasted 36 h at an average rate of about 95 m^3/h. Stope samples reached 2.8–2.9 MPa after 35 d.

Table 1. Representative formulations, test conditions and reported performance in SS-containing mine backfill.

Study	Material System	Test Conditions	Reported Performance	Context
Liu et al. [15]	SS–BFS binder; total tailings, ore type unspecified	Standard mortar; CPB at binder:tailings 1:5–1:10 and 70% solids	28 d: 29.47 MPa mortar; approximately 1.0–2.8 MPa CPB	Binder strength changes substantially on dilution with tailings.
Hao et al. [51]	Cement partly replaced by SS; CPB	0–60% cement replacement; 28 d	8.06 MPa reference; 8.46 MPa at 10% SS	Higher replacement reduced strength and increased peak strain; S60 showed splitting and local shear.
Hao et al. [69]	SS/cement/GBFS/gypsum binder with IOT	52:10:30:8 binder; binder:IOT = 1:4; 28 d at 20–80 °C	3.94, 5.11 and 2.87 MPa at 20, 60 and 80 °C	Sustained elevated-temperature curing; greatest tested strength at 60 °C.
Su et al. [23]	40% OPC/30% metakaolin/30% SS or carbonated SS; IOT	Binder:tailings 1:6; 68% solids; 28 d	CRMB0/CRMB2: 3.30/4.11 MPa; OPC: 3.90 MPa	CRMB2 combined maximum tested strength with maximum measured yield stress and viscosity.
Xiao et al. [92]	SS–GBFS–gypsum binder; tailings backfill	Long-term tests, 28–365 d	UCS: 3.55 to approximately 5.5 MPa; MIP-derived porosity: 29.81 to 46.86%	Continued strength gain accompanied pore coarsening.
Yang et al. [103]	SS-based binder; tailings backfill	Selected mixture: binder:tailings 1:4; 72% solids; validation test	28 d: 3.61 MPa; slump 24.2 cm; bleeding 5.91%	Reported cost 113 CNY m^{-3} versus 185 CNY m^{-3} for cement reference.
Cai et al. [17]	SS/desulfurization ash/GBFS with IOT; SS and ash each 20% of binder	72% solids; 30 m loop, 0.1 m pipe; 0.5/0.6 m s^{-1}	28 d: 5.90 MPa; reported loop-derived yield stress 134.2 Pa and viscosity 2.96 Pa·s	Reported parameters imply higher straight-pipe resistance than OPC at matched diameter and velocity within the adopted Bingham approximation.
Hu et al. [105]	SS-containing binder; ultrafine tailings	Median size approximately 21.2 μm; binder:tailings 1:4; 58–60% solids	36 h continuous filling at approximately 95 m^3 h^{-1}; 35 d: 2.8–2.9 MPa	Thickening, storage and two-stage mixing enabled continuous operation.

Values are study-specific. Binder proportions are mass fractions unless stated otherwise; tailings ore type is identified only where reported. MIP denotes mercury intrusion porosimetry.

The high-SS application at Macheng Iron Mine included mixing, filling, dewatering and inspection of the placed backfill [52]. Local cracks were observed despite satisfactory compressive strength. The field observations complement the ultrafine-tailings operating record: slurry preparation and placement affect both continuity of filling and the condition of the hardened material.

5.2. Equivalent-Function Assessment and Treatment Decision

Environmental and economic selection should compare one cubic meter of backfill meeting the specified age-dependent strength, transportability and service requirements. An untreated or minimally processed formulation establishes the baseline; treatment is valuable when its additional burden is offset by improved performance or reduced binder demand [106–108].

Su et al. [23] estimated CO_2 emissions per kilogram of binder 55.5% below OPC for the untreated OPC–metakaolin–SS blend and 57.6–60.2% below OPC after pre-carbonation. Relative to the same OPC baseline, the additional reduction attributable to treatment is therefore 2.1–4.7 percentage points. Most of the estimated saving comes from formulation

substitution. These constituent-factor estimates credit CO_2 uptake but do not quantify carbonation, gas-supply or drying energy and cost. CRMB2 combined the highest 28 d strength with the highest measured yield stress and plastic viscosity in the series. Treatment selection must therefore weigh the incremental carbon saving against process burdens and the strength–flow trade-off.

Yang et al. reported a backfill cost of 113 CNY m^{-3} versus 185 CNY m^{-3} for the cement reference, a 38.92% reduction, while meeting the specified 7 and 28 d strength, slump and bleeding constraints [103]. This establishes a cost benefit at acceptable performance. Carbon performance requires a separate inventory of constituent production, activator use and transport [108–111].

In an SS–GBFS–fly-ash paste assessment with a 1 m^3 functional unit, sodium silicate and NaOH supplied 34–35% and 28–29% of global warming potential (GWP), respectively, at 8% alkali equivalent [110]. Stronger activation therefore carries an upstream emissions burden that must be weighed against any reduction in binder demand.

A regional LCA for sulfide-tailings backfill provides a combined comparison [108]. Its 1 m^3 boundary covered binder production, admixture, 1000 km haulage and plant energy, excluding tailings generation. Calcined magnesite residue and OPC gave 48.5 and 131 kg CO_2-eq m^{-3}, with purchase, transport and energy costs of 5.01 and 16.61 EUR m^{-3}. Adding monetized environmental damage increased the totals to 14.06 and 34.5 EUR m^{-3}. Their pooled UCS means were 1.55 and 2.92 MPa; NaOH had lower emissions (18.4 kg CO_2-eq m^{-3}) but a mean UCS of 0.33 MPa, below the study's 0.5 MPa requirement. This comparison shows how binder demand and functional adequacy can reverse a per-kilogram material ranking.

Table 2 translates the preceding comparisons into selection criteria. The recurring implication is to select a formulation against the controlling requirement rather than maximize strength, fineness or activation individually. Figure 14 places this assessment after feedstock diagnosis and functional screening. Qualified mixtures can then be compared on binder demand, treatment and transport burdens, and cost before loop/pilot and field validation.

Table 2. Comparative synthesis linking material response to engineering selection.

Comparison	Evidence	Combined Interpretation	Selection Criterion
Activator response	TEA improved one IOT–SS composite mortar; NaOH/sodium silicate reduced strength in another [12,21].	Reaction enhancement depends on precursor balance and existing solution chemistry.	Optimize dosage in the complete blend against sustained strength development.
Pores and strength	Long-term CPB strength increased with MIP pore coarsening; a separate concrete study showed interface densification despite coarser matrix pores [22,92].	Age-related strength–pore divergence and spatial pore heterogeneity require different explanations.	Match pore, contact and crack observations to mechanical tests at the same age and curing conditions.
Strength and deformation	Higher SS contents gave gentler post-peak decline but lower UCS; conventional CPB studies distinguish strength envelopes from post-peak response [51,94,95].	Peak capacity and resistance during continued deformation are separate requirements.	Use target peak strength and stress retention under the relevant stress path.
Rheology and transport	Within the tested blend series, increasing SS raised yield stress and reduced plastic viscosity [17].	Pressure gradient depends on the competing terms and pipe conditions in the Bingham approximation.	Compare both parameters from comparable measurements at the intended diameter and velocity [104].
Pre-carbonation value	The untreated blend provided most estimated carbon reduction; intermediate carbonation maximized strength and flow resistance [23].	Formulation substitution, extra treatment and transport demand make distinct contributions.	Select treatment using incremental savings, required performance and the process inventory.

Author synthesis. The material systems and test conditions are detailed in Sections 2–5.

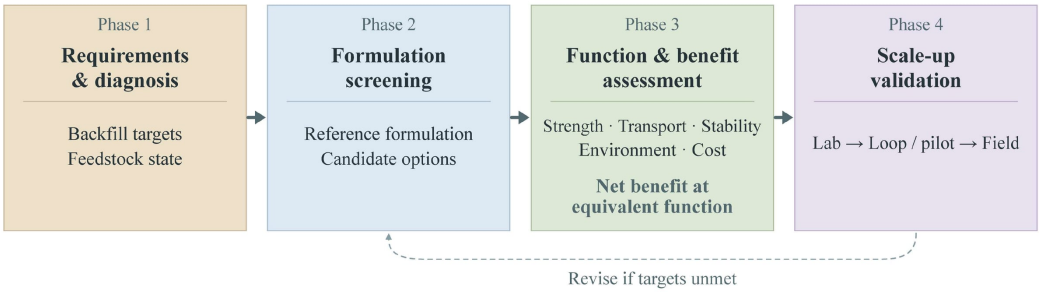


Figure 14. Engineering decision framework: (1) requirements and feedstock diagnosis; (2) formulation screening; (3) function and net-benefit assessment; (4) scale-up validation.

5.3. Field Validation and Future Research Needs

Few studies follow one formulation through laboratory characterization, transport trials and mine placement. Doing so would show whether changes in solids concentration and slurry handling preserve the laboratory strength advantage after pumping and placement. Pressure loss, operating continuity and service-age performance are particularly useful measurements along this sequence.

Life-cycle results are sensitive to binder and activator selection [112]. For backfill, inventories tied to a placed volume meeting specified strength and transport requirements would make treatment comparisons more relevant to mine operation. The formulation changes needed to maintain that performance belong in the inventory together with the treatment itself.

Isolating the IOT reaction requires matched solid- and solution-phase measurements. Future studies should pair time-resolved inductively coupled plasma optical emission or mass spectrometry (ICP-OES/ICP-MS) with quantitative XRD using an internal standard and backscattered-electron imaging with energy-dispersive spectroscopy (BSE–EDS) of identified IOT grains. IOT-only leaching, size-matched low-reactivity filler controls and precursor-only controls under comparable solution conditions would help separate mineral dissolution, packing effects and Si/Al supplied by SS or GBFS. Element balances should include both dissolved and precipitated fractions because solution concentrations reflect release and uptake [36]. Solid-state $^{29}Si/^{27}Al$ nuclear magnetic resonance can complement this analysis by tracking silicate/aluminate environments [86]. Combining these observations would constrain the IOT-derived reaction fraction and its contribution to binder demand and strength.

High-SS systems need longer observations of volume change, cracking and retained strength [52,92]. Tests beyond 28 d should relate these properties to shrinkage, creep and sulfate exposure over the intended service period [113]. Representative mine water is also needed in leaching tests so that environmental performance is evaluated under relevant exposure conditions [3,114].

6. Conclusions

(1) SS and IOT contribute through complementary chemical and particle functions. SS supplies calcium-bearing hydraulic phases and alkalinity; IOT forms the granular skeleton and provides microfilling and hydrate-bearing interfaces. The reaction of accessible tailing fractions can coexist with these physical functions. Binder composition, mineralogy and particle-size distribution jointly determine their contribution.

(2) Mechanical activation improves particle contact and mineral accessibility, but prolonged grinding can produce agglomeration and little additional strength. Chemical activation is formulation-dependent: TEA enhanced one cement-containing blend,

whereas NaOH and sodium silicate lowered strength in another. Thermal reconstruction, elevated-temperature curing and slag pre-carbonation modify different stages of precursor preparation and hydration.

(3) Hardening proceeds through the coupled development of silicate gels, ettringite and other aluminate or carbonate-bearing hydrates. Their composition, intergrowth and interfacial distribution connect treatment to mechanical performance. In the reviewed OPC–metakaolin–SS pre-carbonation series, 28-day backfill strength increased from 3.30 to 4.11 MPa, alongside increases of 22.1% and 41.3% in the elastic moduli of LD and HD C–S–H-associated populations. This case links precursor modification with subsequent gel micromechanics and composite strength.

(4) Bulk pore indicators, peak strength and individual rheological parameters capture different aspects of performance. Strength growth despite pore coarsening requires joint assessment of pore structure, bonded contacts and cracking at matched ages. Gentler post-peak decline can accompany lower peak capacity, so strength and stress retention at the required deformation must be considered together. For pipeline transport, increasing yield stress and decreasing plastic viscosity act in opposite directions; the net pressure-gradient change depends on both parameters, pipe diameter and velocity within the adopted Bingham approximation.

(5) Engineering selection should screen formulations against required strength, deformation, transportability and stability before comparing costs and environmental burdens. In the reviewed pre-carbonation series, most estimated carbon reduction came from composite-binder substitution; additional slag treatment contributed 2.1–4.7 percentage points relative to the same OPC baseline. That increment should be weighed against process inputs, binder demand and the strength–flow trade-off. Pipeline-loop and field tests then establish whether selected formulations retain their laboratory advantages during transport, placement and service.

Supplementary Materials: The following supporting information can be downloaded at: https://www.mdpi.com/article/10.3390/gels12111039/s1, Supplementary Data S1: literature-search methods, screening records, annual publication and citation statistics.

Author Contributions: Conceptualization, Z.N., F.N. and S.Z.; methodology, Z.N. and F.N.; investigation, Z.N., J.Z., K.L., Z.Y., Y.Z. and Z.C.; data curation, Z.N., J.Z., Z.Y., Y.Z. and Z.C.; writing—original draft preparation, Z.N.; writing—review and editing, F.N., J.Z., K.L. and S.Z.; visualization, Z.N., Z.Y. and Y.Z.; supervision, F.N. and S.Z.; project administration, F.N. and J.Z.; funding acquisition, F.N. and S.Z. All authors have read and agreed to the published version of the manuscript.

Funding: This research was funded by the Jing-Jin-Ji Regional Integrated Environmental Improvement-National Science and Technology Major Project [Grant Number 2025ZD1202700], and the S&T Program of Hebei (Supported by Project of Yanzhao Iron and Steel Laboratory, 25363801D).

Institutional Review Board Statement: Not applicable.

Informed Consent Statement: Not applicable.

Data Availability Statement: No new experimental data were generated in this review. The bibliometric search strategy, screened records, inclusion decisions, annual publication counts and citation snapshot are provided in Supplementary Data S1. Experimental evidence discussed in the review is available in the cited publications. Figure source information is provided in the corresponding captions.

Acknowledgments: During manuscript preparation, ChatGPT-5 and Codex (OpenAI), both using the GPT-6 Astra model, were used to assist with language translation. The authors reviewed and edited the output and take full responsibility for the final submitted content.

Conflicts of Interest: The authors declare no conflicts of interest.

References

1. Chang, Q.; Chen, J.; Zhou, H.; Bai, J. Implementation of Paste Backfill Mining Technology in Chinese Coal Mines. *Sci. World J.* **2014**, *2014*, 821025. [CrossRef] [PubMed]
2. Qiu, J.; Zhao, Y.; Long, H.; Guo, Z.; Xing, J.; Sun, X. Low-Carbon Binder for Cemented Paste Backfill: Flowability, Strength and Leaching Characteristics. *Minerals* **2019**, *9*, 707. [CrossRef]
3. Zhang, Q.; Tao, Y.; Feng, Y.; Chen, Q.; Gao, L.; Zhang, Y.; Wang, D. Review on Preparation and Comprehensive Performance Research of Cemented Paste Backfill for Solid Waste from Mining, Beneficiation, Metallurgy and Chemical Industries. *Coal Sci. Technol.* **2025**, *53*, 65–81. [CrossRef]
4. Wang, J.; Xiao, B.; Liu, X.; Ruan, Z. Trends and Applications of Green Binder Materials for Cemented Paste Backfill Mining in China. *Minerals* **2025**, *15*, 97. [CrossRef]
5. Na, H.; Wang, Y.; Zhang, X.; Li, J.; Zeng, Y.; Liu, P. Hydration Activity and Carbonation Characteristics of Dicalcium Silicate in Steel Slag: A Review. *Metals* **2021**, *11*, 1580. [CrossRef]
6. Hao, J.; Zhou, Z.; Chen, Z.; Che, Z.; Wang, X. Review of Hydration and Hardening Properties of Steel Slag in Mine Filling Cementitious Materials. *J. Min. Sci. Technol.* **2024**, *9*, 573–585. [CrossRef]
7. Wan, Y.; Liu, W.; Liu, X.; Mai, Q.; Li, H.; Zhao, P.; Zhang, J.; Xu, S. Activation Methods and Performance of Steel Slag–Granulated Blast Furnace Slag Cementitious Materials: A Review. *Case Stud. Constr. Mater.* **2026**, *24*, e05840. [CrossRef]
8. Hao, J.; Fang, K.; Zhou, Z.; Zhuang, S. Advances in Steel Slag Modification and Synergistic Mechanisms via Multi-Source Solid Waste Integration for Performance Enhancement. *ZKG Int.* **2026**, *79*, 34–53. [CrossRef]
9. Jiang, Y.; Ling, T.-C.; Shi, C.; Pan, S.-Y. Characteristics of Steel Slags and Their Use in Cement and Concrete—A Review. *Resour. Conserv. Recycl.* **2018**, *136*, 187–197. [CrossRef]
10. Zhao, J.; Wang, D.; Yan, P.; Li, W. Comparison of Grinding Characteristics of Converter Steel Slag with and without Pretreatment and Grinding Aids. *Appl. Sci.* **2016**, *6*, 237. [CrossRef]
11. Wang, H.; Gu, X.; Liu, J.; Zhu, Z.; Wang, S.; Xu, X.; Meng, J. Enhancement Mechanism of Micro-Iron Ore Tailings on Mechanical Properties and Hydration Characteristics of Cement-Steel Slag System. *J. Build. Eng.* **2023**, *79*, 107882. [CrossRef]
12. Hu, Z.; Gu, X.; Cheng, B.; Wang, Q.; Liu, J.; Ge, X.; Yin, S. The Role of Chemical Activation in Strengthening Iron Ore Tailings Supplementary Cementitious Materials. *Buildings* **2024**, *14*, 963. [CrossRef]
13. Liu, Y.; Yang, G.; Zhang, S.; Cao, D.; Zhang, G.; Li, Z.; Zhang, C. A Review on the Resource Utilization of Iron Tailings: Pathways, Challenges, and Prospects. *Minerals* **2026**, *16*, 455. [CrossRef]
14. Zhao, Y.; Ma, Z.; Qiu, J.; Sun, X.; Gu, X. Experimental Study on the Utilization of Steel Slag for Cemented Ultra-Fine Tailings Backfill. *Powder Technol.* **2020**, *375*, 284–291. [CrossRef]
15. Liu, M.; Feng, Y.; Zhao, F. Steel Slag/Blast-Furnace Slag Blend Cementing Material for Total Tailings Paste Backfill. *Iron Steel* **2017**, *52*, 89–95+103. [CrossRef]
16. Xiao, B.; Wu, A.; Wang, J. Towards Understanding the Hydration and Hardening Properties of the Cemented Paste Backfill with a Green Steel-Slag Binder. *Int. J. Min. Reclam. Environ.* **2023**, *37*, 769–779. [CrossRef]
17. Cai, J.; Sun, C.; Zhang, J.; Wang, B.; Ran, J.; Tang, N. Study on the Rheological Properties and Microstructural Evolution Mechanism of Multicomponent Solid Waste Cementitious Slurry. *Materials* **2026**, *19*, 994. [CrossRef] [PubMed]
18. Zhang, M.; Li, K.; Ni, W.; Zhang, S.; Liu, Z.; Wang, K.; Wei, X.; Yu, Y. Preparation of Mine Backfilling from Steel Slag-Based Non-Clinker Combined with Ultra-Fine Tailing. *Constr. Build. Mater.* **2022**, *320*, 126248. [CrossRef]
19. Xu, J.; Chen, P. Synergistic Effect of Iron Tailings, Steel Slag and Red Mud Cementitious Materials on Mechanical and Microstructure Properties. *J. Build. Eng.* **2024**, *95*, 110131. [CrossRef]
20. Hu, Z.; Gu, X.; Liu, J.; Ge, X.; Wang, S.; Yin, S. Mechanical Properties and Hydration Mechanism of Iron Tailings–Cement-Based Supplementary Cementitious Materials. *Buildings* **2024**, *14*, 1044. [CrossRef]
21. Zhang, Y.; Sun, H.; Gu, X.; Zhang, W.; Liu, B. Experimental Study on the Use of Iron Tailings-Based Multicomponent Solid Waste as SCMs. *Sustainability* **2022**, *14*, 5124. [CrossRef]
22. Zhang, Y.; Yang, D.; Gu, X.; Chen, H.; Li, Z. Application of Iron Tailings-Based Composite Supplementary Cementitious Materials (SCMs) in Green Concrete. *Materials* **2022**, *15*, 3866. [CrossRef] [PubMed]
23. Su, B.; Yue, X.; Shao, N.; Sun, Y.; Wang, L.; Liu, X.; Qiu, J.; Zhao, Y. CO2-Driven Structural Transformation of Steel Slag into Low-Carbon Cementitious Materials for Carbon-Reducing Mine Backfill. *Int. J. Miner. Metall. Mater.* **2026**, *33*, 2255–2270. [CrossRef]
24. Gou, M.; Zhou, L.; Then, N.W.Y. Utilization of Tailings in Cement and Concrete: A Review. *Sci. Eng. Compos. Mater.* **2019**, *26*, 449–464. [CrossRef]
25. Zhao, J.; Ni, K.; Su, Y.; Shi, Y. An Evaluation of Iron Ore Tailings Characteristics and Iron Ore Tailings Concrete Properties. *Constr. Build. Mater.* **2021**, *286*, 122968. [CrossRef]
26. Zhao, X.; Zhang, Y. Analyzing the Mechanical and Durability Characteristics of Steel Slag-Infused Asphalt Concrete in Roadway Construction. *Buildings* **2024**, *14*, 679. [CrossRef]

27. Tomwsulcer Mortar Mixed Inside Bucket.Jpg. Available online: https://commons.wikimedia.org/wiki/File:Mortar_mixed_inside_bucket.jpg (accessed on 20 September 2026).
28. Xb-70 Failed Concrete Cylinder.jpg. Available online: https://commons.wikimedia.org/wiki/File:Failed_Concrete_Cylinder.jpg (accessed on 20 September 2026).
29. Cacciuttolo, C.; Marinovic, A. Experiences of Underground Mine Backfilling Using Mine Tailings Developed in the Andean Region of Peru: A Green Mining Solution to Reduce Socio-Environmental Impacts. *Sustainability* **2023**, *15*, 12912. [CrossRef]
30. Yildirim, I.Z.; Prezzi, M. Chemical, Mineralogical, and Morphological Properties of Steel Slag. *Adv. Civ. Eng.* **2011**, *2011*, 463638. [CrossRef]
31. Zhuang, S.; Wang, Q. Inhibition Mechanisms of Steel Slag on the Early-Age Hydration of Cement. *Cem. Concr. Res.* **2021**, *140*, 106283. [CrossRef]
32. Zhuang, S.; Wang, Q.; Luo, T. Effect of C12A7 in Steel Slag on the Early-Age Hydration of Cement. *Cem. Concr. Res.* **2022**, *162*, 107010. [CrossRef]
33. Lizarazo-Marriaga, J.; Claisse, P.; Ganjian, E. Effect of Steel Slag and Portland Cement in the Rate of Hydration and Strength of Blast Furnace Slag Pastes. *J. Mater. Civ. Eng.* **2011**, *23*, 153–160. [CrossRef]
34. Carmignano, O.R.; Vieira, S.S.; Teixeira, A.P.C.; Lameiras, F.S.; Brandão, P.R.G.; Lago, R.M. Iron Ore Tailings: Characterization and Applications. *J. Braz. Chem. Soc.* **2021**, *32*, 1895–1911. [CrossRef]
35. Wang, C.; Jing, J.; Qi, Y.; Zhou, Y.; Zhang, K.; Zheng, Y.; Zhai, Y.; Liu, F. Basic Characteristics and Environmental Impact of Iron Ore Tailings. *Front. Earth Sci.* **2023**, *11*, 1181984. [CrossRef]
36. Obenaus-Emler, R.; Falah, M.; Illikainen, M. Assessment of Mine Tailings as Precursors for Alkali-Activated Materials for on-Site Applications. *Constr. Build. Mater.* **2020**, *246*, 118470. [CrossRef]
37. Zhang, S.; Wu, B.; Ren, Y.; Wu, Z.; Li, Q.; Li, K.; Zhang, M.; Yu, J.; Liu, J.; Ni, W. The Preparation Process and Hydration Mechanism of Steel Slag-Based Ultra-Fine Tailing Cementitious Filler. *Gels* **2023**, *9*, 82. [CrossRef] [PubMed]
38. Wang, H.; Gu, X.; Xu, X.; Liu, J.; Zhu, Z.; Wang, S. The Effects of Iron Tailings on Steel Slag-Based Cementitious Systems: Strength, Hydration Products, and Volume Stability. *J. Build. Eng.* **2024**, *91*, 109702. [CrossRef]
39. Shettima, A.U.; Hussin, M.W.; Ahmad, Y.; Mirza, J. Evaluation of Iron Ore Tailings as Replacement for Fine Aggregate in Concrete. *Constr. Build. Mater.* **2016**, *120*, 72–79. [CrossRef]
40. Yang, Y.; Chen, L.; Mao, Y. Different Effects of Wet and Dry Grinding on the Activation of Iron Ore Tailings. *J. Renew. Mater.* **2021**, *9*, 2261–2276. [CrossRef]
41. Cheng, Y.; Tong, B.; Sun, X.; Zhang, J. On the Grinding Effects of High-Silicon Iron Tailings. *Environ. Sci. Pollut. Res.* **2022**, *29*, 73326–73340. [CrossRef] [PubMed]
42. Wang, C.; Qi, Y.; Jing, J.; Ma, J.; Zhou, Y.; Ping, H.; Zheng, Y.; Zhai, Y.; Liu, F. Properties and Microstructure of Total Tailings Cemented Paste Backfill Material Containing Mining and Metallurgical Solid Waste. *Front. Earth Sci.* **2023**, *11*, 1181952. [CrossRef]
43. Cai, J.; Sun, C.; Zhang, J.; Cheng, X.; Tang, N. Mix Design Optimization and Performance Prediction of Multi-Source Solid Waste-Based Backfill Materials Using Response Surface Methodology and BP Neural Network. *Results Eng.* **2026**, *29*, 108761. [CrossRef]
44. Li, Q.; Wang, B.; Yang, L.; Zhou, H.; Kang, M.; Li, R.; Shu, X. Synthesis of Cemented Paste Backfill by Reutilizing Multiple Industrial Waste Residues and Ultrafine Tailings: Strength, Microstructure, and GA-GPR Prediction Modeling. *Powder Technol.* **2024**, *434*, 119337. [CrossRef]
45. Ling, G.; Shui, Z.; Gao, X.; Sun, T.; Yu, R.; Li, X. Utilizing Iron Ore Tailing as Cementitious Material for Eco-Friendly Design of Ultra-High Performance Concrete (UHPC). *Materials* **2021**, *14*, 1829. [CrossRef] [PubMed]
46. Cui, L.; Chen, P.; Wang, L.; Xu, Y.; Wang, H. Reutilizing Waste Iron Tailing Powders as Filler in Mortar to Realize Cement Reduction and Strength Enhancement. *Materials* **2022**, *15*, 541. [CrossRef] [PubMed]
47. Yao, G.; Wang, Q.; Su, Y.; Wang, J.; Qiu, J.; Lyu, X. Mechanical Activation as an Innovative Approach for the Preparation of Pozzolan from Iron Ore Tailings. *Miner. Eng.* **2020**, *145*, 106068. [CrossRef]
48. Yao, G.; Wang, Q.; Wang, Z.; Wang, J.; Lyu, X. Activation of Hydration Properties of Iron Ore Tailings and Their Application as Supplementary Cementitious Materials in Cement. *Powder Technol.* **2020**, *360*, 863–871. [CrossRef]
49. Yang, Y.; Yang, Z.; Cheng, Z.; Zhang, H. Effects of Wet Grinding Combined with Chemical Activation on the Activity of Iron Tailings Powder. *Case Stud. Constr. Mater.* **2022**, *17*, e01385. [CrossRef]
50. Figueiredo, R.A.M.; Silveira, A.B.M.; Melo, E.L.P.; Costa, G.Q.G.; Brandão, P.R.G.; Aguilar, M.T.P.; Henriques, A.B.; Mazzinghy, D.B. Mechanical and Chemical Analysis of One-Part Geopolymers Synthesised with Iron Ore Tailings from Brazil. *J. Mater. Res. Technol.* **2021**, *14*, 2650–2657. [CrossRef]
51. Hao, J.; Zhou, Z.; Chen, Z.; Zhou, Y.; Wang, J. Damage Characterization and Microscopic Mechanism of Steel Slag-Cemented Paste Backfill under Uniaxial Compression. *Constr. Build. Mater.* **2023**, *409*, 134175. [CrossRef]

52. Hao, J.; Zhou, Z.; Chen, Z.; Jia, R.; Zhuang, S.; Fang, K.; Tang, F.; Song, Z. Utilization of High-Volume Steel Slag in Sustainable Low Carbon Cementitious Composites for Mine Backfill: Synergistic Mechanisms and Environmental Benefits. *Process Saf. Environ. Prot.* **2025**, *202*, 107689. [CrossRef]
53. Xiao, B.; Huang, H.; Zhang, J. A Green Sintering-Free Binder Material with High-Volumetric Steel Slag Dosage for Mine Backfill. *Minerals* **2022**, *12*, 1036. [CrossRef]
54. Wang, Q.; Yan, P.; Mi, G. Effect of Blended Steel Slag–GBFS Mineral Admixture on Hydration and Strength of Cement. *Constr. Build. Mater.* **2012**, *35*, 8–14. [CrossRef]
55. Fathy, S.; Liping, G.; Ma, R.; Chunping, G.; Wei, S. Comparison of Hydration Properties of Cement-Carbon Steel Slag and Cement-Stainless Steel Slag Blended Binder. *Adv. Mater. Sci. Eng.* **2018**, *2018*, 1851367. [CrossRef]
56. Kourounis, S.; Tsivilis, S.; Tsakiridis, P.E.; Papadimitriou, G.D.; Tsibouki, Z. Properties and Hydration of Blended Cements with Steelmaking Slag. *Cem. Concr. Res.* **2007**, *37*, 815–822. [CrossRef]
57. Zhang, Z.; Lian, F.; Liao, H.; Yang, Q.; Cao, W. Modifying the Properties of Steel Slag by Iron Tailings at High Temperature. *J. Univ. Sci. Technol. Beijing* **2012**, *34*, 1379–1384. [CrossRef]
58. Zhang, Y.; Liu, B.; Gu, X.; Nehdi, M.L.; Zhang, L.V. Mechanochemical Activation of Iron Ore Tailing-Based Ternary Supplementary Cementitious Materials. *Constr. Build. Mater.* **2022**, *346*, 128420. [CrossRef]
59. Gu, X.; Zhang, W.; Zhang, X.; Li, X.; Qiu, J. Hydration Characteristics Investigation of Iron Tailings Blended Ultra High Performance Concrete: The Effects of Mechanical Activation and Iron Tailings Content. *J. Build. Eng.* **2022**, *45*, 103459. [CrossRef]
60. Kumar, A.; Oey, T.; Falzone, G.; Huang, J.; Bauchy, M.; Balonis, M.; Neithalath, N.; Bullard, J.; Sant, G. The Filler Effect: The Influence of Filler Content and Type on the Hydration Rate of Tricalcium Silicate. *J. Am. Ceram. Soc.* **2017**, *100*, 3316–3328. [CrossRef]
61. Cui, H.; Wang, C.; Zhang, G.; Zhang, K.; Fu, X.; Bai, Y.; Zheng, Y.; Qi, Y.; Liu, Z. Preparation and Hydration Mechanism of Composite Cementitious Materials Based on Iron and Steel Solid Waste. *Alex. Eng. J.* **2024**, *103*, 343–352. [CrossRef]
62. Xue, G.; Yilmaz, E.; Song, W.; Cao, S. Compressive Strength Characteristics of Cemented Tailings Backfill with Alkali-Activated Slag. *Appl. Sci.* **2018**, *8*, 1537. [CrossRef]
63. Ouyang, S.; Huang, Y.; Wu, L.; Yin, W.; Yang, X.; Wang, J.; Wang, G.; Li, J.; Lei, Y. Effects of Chlorides on Setting Time, Hydration Heat and Hydration Products of Fresh Slurry of Cemented Paste Backfill. *Case Stud. Constr. Mater.* **2022**, *17*, e01462. [CrossRef]
64. Sun, Q.; Li, T.; Liang, B. Preparation of a New Type of Cemented Paste Backfill with an Alkali-Activated Silica Fume and Slag Composite Binder. *Materials* **2020**, *13*, 372. [CrossRef] [PubMed]
65. Pontikes, Y.; Kriskova, L.; Cizer, Ö.; Jones, P.T.; Blanpain, B. On a New Hydraulic Binder from Stainless Steel Converter Slag. *Adv. Cem. Res.* **2013**, *25*, 21–31. [CrossRef]
66. Lian, F.; Ma, L.; Chou, K. Industrial Research on the High-Temperature Modification of Basic Oxygen Furnace Slag with Solid Waste Compound. *J. Clean. Prod.* **2017**, *143*, 549–556. [CrossRef]
67. Wang, C.; Zhao, G.; Zheng, Y.; Zhang, K.; Ye, P.; Cui, X. Study on the Preparation of High Performance Concrete Using Steel Slag and Iron Ore Tailings. *J. New Mater. Electrochem. Syst.* **2019**, *22*, 217–223. [CrossRef]
68. Walske, M.L.; McWilliam, H.; Doherty, J.; Fourie, A. Influence of Curing Temperature and Stress Conditions on Mechanical Properties of Cementing Paste Backfill. *Can. Geotech. J.* **2016**, *53*, 148–161. [CrossRef]
69. Hao, J.; Zhou, Z.; Chen, Z.; Zhao, Z.; Shen, Y. Mechanical Performance and Damage Mechanisms of Steel Slag-Cement Pasted Backfill under High-Temperature Cured and Cyclic Static Loading for Deep-Mining Applications. *J. Mater. Res. Technol.* **2025**, *35*, 5698–5716. [CrossRef]
70. He, Z.; Yang, H.; Shao, Y.; Liu, M. Early Carbonation Behaviour of No-Clinker Steel Slag Binder. *Adv. Cem. Res.* **2013**, *25*, 342–351. [CrossRef]
71. Liu, P.; Zhang, M.; Mo, L.; Zhong, J.; Xu, M.; Deng, M. Probe into Carbonation Mechanism of Steel Slag via FIB-TEM: The Roles of Various Mineral Phases. *Cem. Concr. Res.* **2022**, *162*, 106991. [CrossRef]
72. Abo-El-enein, S.A.; Ata, A.A.; Hassanien, A.; Sh. Mikhai, R. Kinetics and Mechanism of Slag Cement Hydration. *J. Chem. Technol. Biotechnol.* **1982**, *32*, 939–945. [CrossRef]
73. Li, Q.; Wang, B.; Yang, L.; Kang, M. Recycling Multisource Industrial Waste Residues as Green Binder for Cemented Ultrafine Tailings Backfill: Hydration Kinetics, Mechanical Properties, and Solidification Mechanism. *Powder Technol.* **2024**, *441*, 119799. [CrossRef]
74. Han, F.; Zhang, Z.; Wang, D.; Yan, P. Hydration Heat Evolution and Kinetics of Blended Cement Containing Steel Slag at Different Temperatures. *Thermochim. Acta* **2015**, *605*, 43–51. [CrossRef]
75. Zunino, F.; Scrivener, K. Microstructural Developments of Limestone Calcined Clay Cement (LC3) Pastes after Long-Term (3 Years) Hydration. *Cem. Concr. Res.* **2022**, *153*, 106693. [CrossRef]
76. Fathy, S.; Liping, G.; Rui, M.; Chunping, G.; Wei, S. A Comparative Study on Hydraulic Properties and Cementitious Activity of Carbon Steel Slag and Stainless Steel Slag. *J. Test. Eval.* **2019**, *47*, 1–17. [CrossRef]

77. Kunhi Mohamed, A.; Moutzouri, P.; Berruyer, P.; Walder, B.J.; Siramanont, J.; Harris, M.; Negroni, M.; Galmarini, S.C.; Parker, S.C.; Scrivener, K.L.; et al. The Atomic-Level Structure of Cementitious Calcium Aluminate Silicate Hydrate. *J. Am. Chem. Soc.* **2020**, *142*, 11060–11071. [CrossRef] [PubMed]
78. Myers, R.J.; L'Hôpital, E.; Provis, J.L.; Lothenbach, B. Composition–Solubility–Structure Relationships in Calcium (Alkali) Aluminosilicate Hydrate (C-(N,K-)A-S-H). *Dalton Trans.* **2015**, *44*, 13530–13544. [CrossRef] [PubMed]
79. Myers, R.J.; Bernal, S.A.; San Nicolas, R.; Provis, J.L. Generalized Structural Description of Calcium–Sodium Aluminosilicate Hydrate Gels: The Cross-Linked Substituted Tobermorite Model. *Langmuir* **2013**, *29*, 5294–5306. [CrossRef] [PubMed]
80. Tang, Y.; Zheng, J.; Guo, L.; Zhao, Y. Effect of Gypsum Addition on the Mechanical and Microstructural Performance of Sulphide-Rich Cemented Paste Backfill. *Minerals* **2021**, *11*, 283. [CrossRef]
81. Hemstad, P.; Lothenbach, B.; De Weerdt, K. Distribution of Sulphate and Aluminium in Hydrated Cement Pastes. *Cem. Concr. Res.* **2024**, *180*, 107467. [CrossRef]
82. Zunino, F.; Scrivener, K. The Reaction between Metakaolin and Limestone and Its Effect in Porosity Refinement and Mechanical Properties. *Cem. Concr. Res.* **2021**, *140*, 106307. [CrossRef]
83. Parashar, A.; Bishnoi, S. Hydration Behaviour of Limestone-Calcined Clay and Limestone-Slag Blends in Ternary Cement. *RILEM Tech. Lett.* **2021**, *6*, 17–24. [CrossRef]
84. Geng, G.; Myers, R.J.; Li, J.; Maboudian, R.; Carraro, C.; Shapiro, D.A.; Monteiro, P.J.M. Aluminum-Induced Dreierketten Chain Cross-Links Increase the Mechanical Properties of Nanocrystalline Calcium Aluminosilicate Hydrate. *Sci. Rep.* **2017**, *7*, 44032. [CrossRef] [PubMed]
85. Geng, G.; Myers, R.J.; Qomi, M.J.A.; Monteiro, P.J.M. Densification of the Interlayer Spacing Governs the Nanomechanical Properties of Calcium-Silicate-Hydrate. *Sci. Rep.* **2017**, *7*, 10986. [CrossRef] [PubMed]
86. Walkley, B.; Provis, J.L. Solid-State Nuclear Magnetic Resonance Spectroscopy of Cements. *Mater. Today Adv.* **2019**, *1*, 100007. [CrossRef]
87. Li, J.; Yu, Q.; Huang, H.; Yin, S. Effects of Ca/Si Ratio, Aluminum and Magnesium on the Carbonation Behavior of Calcium Silicate Hydrate. *Materials* **2019**, *12*, 1268. [CrossRef] [PubMed]
88. Matschei, T.; Lothenbach, B.; Glasser, F.P. The Role of Calcium Carbonate in Cement Hydration. *Cem. Concr. Res.* **2007**, *37*, 551–558. [CrossRef]
89. Li, C.; Zhang, N.; Zhang, J.; Song, S.; Zhang, Y. C-A-S-H Gel and Pore Structure Characteristics of Alkali-Activated Red Mud–Iron Tailings Cementitious Mortar. *Materials* **2022**, *15*, 112. [CrossRef] [PubMed]
90. Ouyang, X.; Koleva, D.A.; Ye, G.; van Breugel, K. Insights into the Mechanisms of Nucleation and Growth of C–S–H on Fillers. *Mater. Struct.* **2017**, *50*, 213. [CrossRef]
91. Rong, H.; Zhou, M.; Hou, H. Pore Structure Evolution and Its Effect on Strength Development of Sulfate-Containing Cemented Paste Backfill. *Minerals* **2017**, *7*, 8. [CrossRef]
92. Xiao, B.; Wen, Z.; Miao, S.; Gao, Q. Utilization of Steel Slag for Cemented Tailings Backfill: Hydration, Strength, Pore Structure, and Cost Analysis. *Case Stud. Constr. Mater.* **2021**, *15*, e00621. [CrossRef]
93. Zhang, C.; Wang, J.; Song, W.; Fu, J. Pore Structure, Mechanical Behavior and Damage Evolution of Cemented Paste Backfill. *J. Mater. Res. Technol.* **2022**, *17*, 2864–2874. [CrossRef]
94. Pan, A.; Grabinsky, M. Mechanical Characterization of Cemented Paste Backfill. *Eng* **2023**, *4*, 738–747. [CrossRef]
95. Pan, A.; Grabinsky, M. Yield Characteristics of Cemented Paste Backfill. *CivilEng* **2022**, *3*, 1053–1060. [CrossRef]
96. Pan, A.N.; Grabinsky, M.W.F. Tensile Strength of Cemented Paste Backfill. *Geotech. Test. J.* **2021**, *44*, 1886–1897. [CrossRef]
97. Pan, A.N.; Grabinsky, M.W.F.; Guo, L. Shear Properties of Cemented Paste Backfill under Low Confining Stress. *Adv. Civ. Eng.* **2021**, *2021*, 7561977. [CrossRef]
98. Zhang, Z.; Li, J. Experimental Investigation on Strength and Failure Characteristics of Cemented Paste Backfill. *Front. Mater.* **2021**, *8*, 792561. [CrossRef]
99. Juckes, L.M. The Volume Stability of Modern Steelmaking Slags. *Miner. Process. Extr. Metall. Trans. Inst. Min. Metall. Sect. C* **2003**, *112*, 177–197. [CrossRef]
100. Zhao, Y.; Taheri, A.; Karakus, M.; Chen, Z.; Deng, A. Effects of Water Content, Water Type and Temperature on the Rheological Behaviour of Slag-Cement and Fly Ash-Cement Paste Backfill. *Int. J. Min. Sci. Technol.* **2020**, *30*, 271–278. [CrossRef]
101. Cao, S.; Yilmaz, E.; Song, W. Evaluation of Viscosity, Strength and Microstructural Properties of Cemented Tailings Backfill. *Minerals* **2018**, *8*, 352. [CrossRef]
102. Yang, L.; Wang, H.; Li, H.; Zhou, X. Effect of High Mixing Intensity on Rheological Properties of Cemented Paste Backfill. *Minerals* **2019**, *9*, 240. [CrossRef]
103. Yang, X.; Yan, Z.; Yin, S.; Li, W.; Gao, Q. Development of Steel-Slag-Based Cementitious Material and Optimization of Slurry Ratio Based on Genetic Algorithm and Support Vector Machine (GA−SVM). *Chin. J. Eng.* **2022**, *44*, 1897–1908. [CrossRef]
104. Gao, R.; Zhou, K.; Zhou, Y.; Yang, C. Research on the Fluid Characteristics of Cemented Backfill Pipeline Transportation of Mineral Processing Tailings. *Alex. Eng. J.* **2020**, *59*, 4409–4426. [CrossRef]

105. Hu, Y.; Chen, Y.; Lai, W.; Bai, X.; Chen, T. Study of Key Technology of Paste-like Green Cemented Filling with Ultra-Fine Ungraded Tailings. *Gold* **2023**, *44*, 12–15. [CrossRef]
106. Jiang, M.; Chen, X.; Rajabipour, F.; Hendrickson, C.T. Comparative Life Cycle Assessment of Conventional, Glass Powder, and Alkali-Activated Slag Concrete and Mortar. *J. Infrastruct. Syst.* **2014**, *20*, 04014020. [CrossRef]
107. Shi, X.; Wang, X.; Wang, X. Dual Waste Utilization in Cemented Paste Backfill Using Steel Slag and Mine Tailings and the Heavy Metals Immobilization Effects. *Powder Technol.* **2022**, *403*, 117413. [CrossRef]
108. Valenzuela-Díaz, M.J.; Diosdado-Aragón, A.J.; Munizaga-Rosas, J.C.; Caraballo, M. Life Cycle Assessment of Portland Cement Alternatives in Mine Paste Backfill. *Appl. Sci.* **2025**, *15*, 9996. [CrossRef]
109. Snellings, R.; Suraneni, P.; Skibsted, J. Future and Emerging Supplementary Cementitious Materials. *Cem. Concr. Res.* **2023**, *171*, 107199. [CrossRef]
110. Ji, X.; Wang, X.; Zhao, X.; Wang, Z.; Zhang, H.; Liu, J. Properties, Microstructure Development and Life Cycle Assessment of Alkali-Activated Materials Containing Steel Slag under Different Alkali Equivalents. *Materials* **2024**, *17*, 48. [CrossRef] [PubMed]
111. Komkova, A.; Habert, G. Environmental Impact Assessment of Alkali-Activated Materials: Examining Impacts of Variability in Constituent Production Processes and Transportation. *Constr. Build. Mater.* **2023**, *363*, 129032. [CrossRef]
112. Faridmehr, I.; Nehdi, M.L.; Nikoo, M.; Huseien, G.F.; Ozbakkaloglu, T. Life-Cycle Assessment of Alkali-Activated Materials Incorporating Industrial Byproducts. *Materials* **2021**, *14*, 2401. [CrossRef] [PubMed]
113. Zhang, S.; Zhao, Y.; Zhang, X.; Wang, K. Durability and Heavy Metals Leaching Behavior of Cemented Paste Backfill Using Chemical Activated Binary Slag as Binder under Sulfate Attack. *Case Stud. Constr. Mater.* **2024**, *20*, e03065. [CrossRef]
114. Su, Z.; Chen, Q.; Zhang, Q.; Zhang, D. Recycling Lead–Zinc Tailings for Cemented Paste Backfill and Stabilisation of Excessive Metal. *Minerals* **2019**, *9*, 710. [CrossRef]

Disclaimer/Publisher's Note: The statements, opinions and data contained in all publications are solely those of the individual author(s) and contributor(s) and not of MDPI and/or the editor(s). MDPI and/or the editor(s) disclaim responsibility for any injury to people or property resulting from any ideas, methods, instructions or products referred to in the content.